Stellar rotation formalisms of γ Doradus stars from gravity-mode period spacings

Cheryl Si Ching Lau

MSc by Research

University of York

Physics

December 2019

Abstract

The oscillation frequencies of stars are used to constrain our theoretical models, from which we can derive stellar internal properties including rotation rates. The g-mode pulsations of γ Doradus stars are highly sensitive to the near-core regions. Two of the most common rotation formalisms, the second-order Perturbative Approach and the Traditional Approximation of Rotation, are compared to investigate their validity domains. We compute grids of 1-D γ Doradus models for (1,0) modes with the two rotation descriptions, using benchmark models instead of real stars to be the targets. Results show that the grids are generally capable of reproducing the benchmark to within observational uncertainties. However, the two formalisms disagree with each other at rotation rates beyond $\Omega/\Omega_k = 0.04$. A method of distinguishing the formalisms without presupposing the stars' rotation rates is successfully found: Their models diverge at periods longer than 2.5 days, given that the gradient of the period spacing is greater than -0.0122. The comparison results also reveal that our method of fitting period spacing series is not sufficient for taking rotational mixing effects fully into account. These findings offer potential for refining our current rotation theories with observational data, and contribute to the development of new techniques for improving modelling accuracies.

Contents

List of Tables

List of Figures

Acknowledgements

I would like to express my deep gratitude to my supervisor, Dr. Emily Brunsden, for her generous support and invaluable guidance on this research work throughout my degree. This thesis would not have been possible without all the advice and helpful comments. Thank you for stopping me from attempting to write a hundred-page book. I would also like to thank Dr. Catherine Lovekin for the insightful discussions during her visit at York. Her suggestions gave new inspirations on the research direction.

The modelling results of the *Kepler* star KIC 4846809, along with those for 611 γ Doradus stars, were kindly provided by Gang Li. I appreciate his step-by-step guide on reading the data files. The simulation code inputs used in this work made use of the MESA Summer School teaching materials on MESA marketplace. I thank Dr. Richard Townsend for the codes in his lab materials, and for his help on resolving issues with installing GYRE.

I gratefully acknowledge the scholarship received from the Department of Physics, University of York, to undertake my MScR degree.

Cheryl Lau

York, December 2019

Declaration

I declare that this thesis is a presentation of original work and I am the sole author. This work has not previously been presented for an award at this, or any other, University. All sources are acknowledged as References.

Chapter 1

Introduction

"All models are wrong, but some are useful."

— George E. P. Box (1976)

The study of astrophysics relies on an accurate theoretical description of stellar internal structures and evolution models. From interstellar dust to the formation of galaxies, stars have a significant influence on their environment as they evolve. Our understanding of the mixing processes and angular momentum transport mechanisms in the stellar interior has a direct impact on other astrophysical research; this includes characterizing planetary systems, modelling galactic evolution and age determination of the Universe. All these modern research domains are dependent on the accuracy and precision of the predictions from models, which are constructed on the basis of numerous formalisms describing the physics inside stars.

Whilst the overall picture of stellar structure is well-understood, the uncertainties in detailed descriptions, such as rotation effects and internal mixings around the stellar core, are yet to be resolved. For example, the observed core-to-surface rotation rates in Red Giant stars were found to be much smaller than predictions, indicating that our current treatment of rotation effects and angular momentum transport requires further calibrations to existing theories (e.g. Eggenberger et al. 2017, Fuller et al. 2019). Thanks to new space missions such as CoRoT (Convection, Rotation and planetary Transits; Auvergne et al. 2009), *Kepler* (Koch et al. 2010), and TESS (Transiting Exoplanet Survey Satellite; Ricker et al. 2015), a rapid growth in high-precision space-based photometry data has led to significant improvements in constraining theoretical models. It is therefore crucial to ensure that our modelling theories and methods are sufficiently accurate for interpreting the observational data, yet computationally inexpensive to allow ensemble modelling.

This thesis explores the various rotation modelling formalisms adopted in current asteroseismic research and investigates their domains of validity. We examine the reliability of our state-of-the-art pulsation modelling methods by studying the γ Doradus variable stars with two different rotation theories - the Second-order Perturbative approach and the Traditional Approximation of Rotation. The probing power of these methods are gauged to determine whether or not our current theoretical frameworks are sufficient for mimicking the observable effects of the internal stellar processes. We aim to develop a method of identifying the more suitable rotation formalisms for γ Doradus stars with their pulsation data, which serves as a means for refining our stellar theories.

The following chapter begins by providing an overview of the asteroseismic modelling theories and techniques for deriving the interior properties of γ Doradus stars. We discuss the shortcomings in the rotation formalisms with the purpose of justifying our motivation to determine the more accurate theoretical description. Chapter 2 outlines our research methodology for quantifying the probing ability of γ Doradus stars models, and identifying differences between the pulsations simulated with each rotation formalism. The results obtained through comparisons amongst the models are presented in Chapter 3. Finally, Chapter 4 draws interpretations regarding the modelling precisions, and concludes the thesis by discussing their implications of the appropriateness of our modern seismic modelling methods.

1.1 Theory of Stellar structure

Stellar modelling codes often make approximations to the physics such that a star's structure can be solely described by the following quantities: mass *M(m)*, luminosity *L(m)*, temperature *T(m)*, density *ρ(m)*, chemical composition X_i*(m)*, and the rate of change in energy *ϵ(m)*, where m is a coordinate system corresponding to the mass distribution inside the star. Equations are formulated based on the assumptions that the star is not rotating, has no magnetic fields, and is spherically symmetric at hydrostatic equilibrium. By applying the conservation laws of mass, energy and momentum, we can then characterize the stellar structure with the following set of differential equations:

$$\frac{\partial r}{\partial m} = \frac{1}{4\pi r^2 \rho}, \tag{1.1}$$

$$\frac{\partial P}{\partial m} = -\frac{Gm}{4\pi r^4}, \tag{1.2}$$

$$\frac{\partial L}{\partial m} = \epsilon_n - \epsilon_\nu + \epsilon_g, \tag{1.3}$$

$$\frac{\partial T}{\partial m} = -\frac{GmT}{4\pi r^4\ P}\nabla, \tag{1.4}$$

$$\frac{\partial X_i}{\partial t} = \frac{m_i}{\rho}\left(\sum_j r_{ji} - \sum_k r_{ik}\right), i = 1, ..., I \tag{1.5}$$

(see e.g. Schmid 2016, Van Reeth 2017), where r is the stellar radius and G is the gravitational constant. Equation 1.1 describes the radial mass distribution within the star. Equation 1.2 describes hydrostatic equilibrium, where the gravitational force acting on the star balances the pressure force generated from within. Parameters ϵ_n and ϵ_g are the rate of energy generation per unit mass by nuclear reactions and gravitational force, whereas ϵ_ν denotes the rate of energy loss due to neutrinos, hence Equation 1.3 describes the rate of change in energy. Equation 1.4 describes the energy transport within the star by radiation and/or convection, and indicates the change in temperature in a macroscopic element as it rises or sinks radially. Mixing Length Theory (MLT; Henyey et al. 1965) is often applied to Equation 1.4 to simulate convection, which assumes that the elements will rise through a certain distance before releasing their heat to the surroundings. We define the mean free path of the macroscopic element as $l_m = \alpha_{MLT} H_P$, where H_P is the local pressure scale height. Convective effects are hence parameterized by the constant of proportionality α_{MLT}. The term ∇ is defined as the temperature gradient with respect to depth. Equation 1.5 illustrates the nuclear reaction network in stars, and describes the change in mass fraction X_i of nucleus of type i. Suppose the nuclear burning process converts nucleus of type j into type i then into type k, r_{ji} represents

the thermonuclear reaction rate in converting nucleus j to i, and r_{ik} is the rate in converting nucleus i to k.

To combine Equations 1.1 to 1.5, we require an Equation of State (EOS) which relates the stellar parameters pressure P, temperature T, density ρ, and chemical composition X_i. Under the assumption that the star is an ideal gas with radiation pressure, the EOS is given by

$$P = \frac{R}{\bar{\mu}}\rho T + \frac{a}{3}T^4 \tag{1.6}$$

(see e.g. Pápics 2013, Schmid 2016, Van Reeth 2017), where $\bar{\mu}$ is the mean molecular weight, R is the ideal gas constant and a is the constant derived from the energy density of an ideal photon gas. The quantities involved are described as functions of P and T.

A stellar model is a mathematical construct which utilizes the EOS for different chemical compositions, and solves the system of differential equations with given initial conditions and parameter boundaries.[1] Since the star is assumed to be spherically symmetrical, we may simply consider the stellar processes and structure along a 1-D line in radial direction, spanning from the centre of star to the surface. Properties associated with each section on the line (mesh) represents the processes within a stellar layer or at the layer boundary. Starting conditions such as chemical composition and stellar mass are required for creating stellar models and subsequently evolving them.

1.2 Introduction to Asteroseismology

As a star evolves, changes in internal conditions and physical processes can cause the star to oscillate around its equilibrium state, leading to variations in luminosity. Almost all types of stars will exhibit pulsation phenomena for at least one phase in their lifetime, with varying degrees of impact on their structure and evolution. However, the most periodic and stable pulsation behaviour occurs when the star crosses the instability strip on the Hertzsprung-Russell (HR) diagram, as shown in Figure 1.1. Stars within the instability strip are classified as classical pulsating stars, and their pulsations are further categorized as radial or non-radial. Examples of radial pulsators include Cepheids and RR Lyrae, which typically oscillate with a single-frequency. Pulsations in these stars are excited due to change in opacities in the helium ionization zone (Eddington 1917), causing them to expand and contract while maintaining a spherically symmetric shape. Stars which exhibit the above-stated oscillation behaviour are said to be pulsating in the fundamental radial mode.

[1] Modern stellar models often use tabulated EOS in order to lower the computational cost. Instead of evaluating the EOS in each call, the root finds are pre-processed, creating tables of density values for a range of gas pressure and temperature values (Paxton et al. 2011).

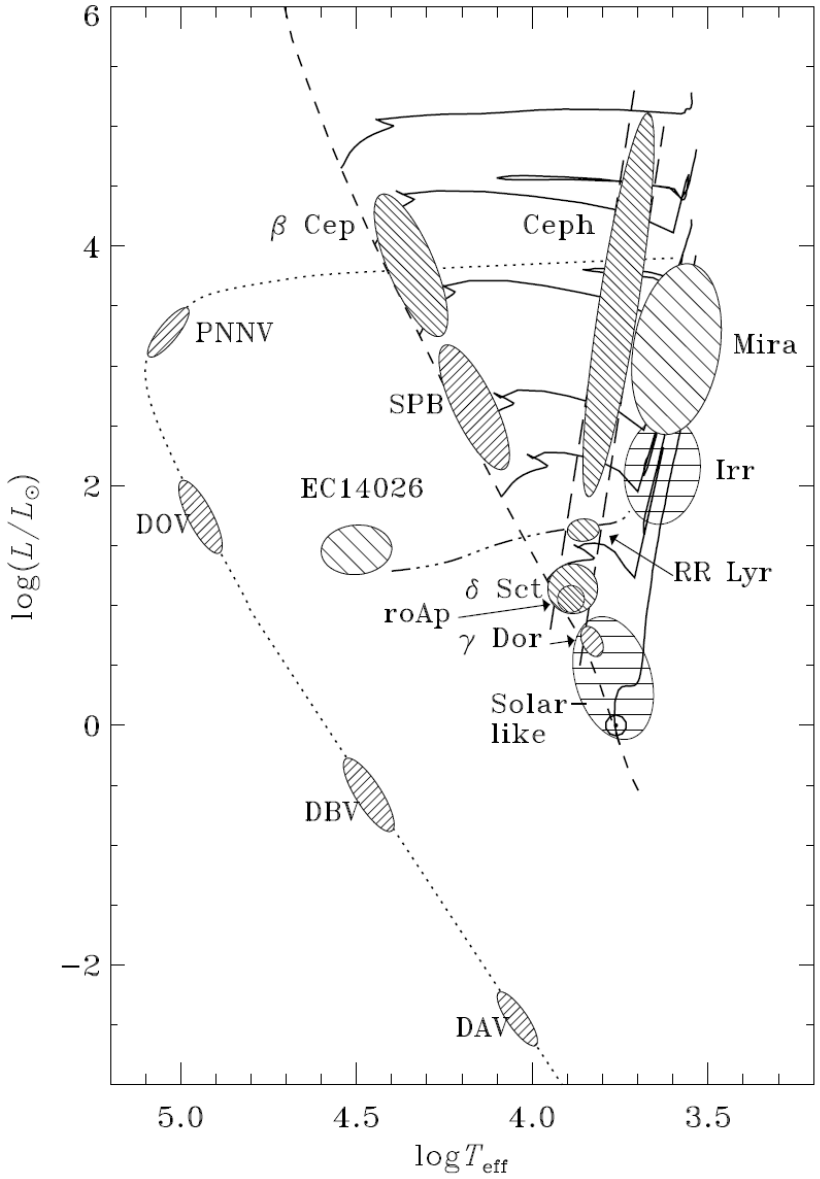

Figure 1.1: Hertzsprung-Russell (HR) diagram illustrating the location of different classes of pulsating stars, including those in the instability strip. The dash-line spanning from top-left to middle-right of the diagram shows the positions of zero-age main sequence stars. The classical instability strip is the region which has one end on the main sequence line and the other end at the top edge of the Cepheid region; its boundaries are indicated by the two parallel dash-lines. The instability strip also includes the δ Scuti stars and the γ Doradus stars. Reprinted from Christensen-Dalsgaard (2003).

Non-radial variable stars are important targets for investigating internal structures and properties. These stars are generally multi-periodic. The pulsations effectively divide the stellar surface into discrete segments comprising of radial and transverse motions. Pulsation modes are characterized by quantum numbers n, l and m to denote the pulsation geometry. Radial order n determines the number of nodal shells in the radial direction, degree l indicates the total number of nodal lines on stellar surface, and the absolute value of azimuthal order m indicates the number of longitudinal nodal lines. Figure 1.2 illustrates the contour plots of stellar surface geometry for different pulsation modes.

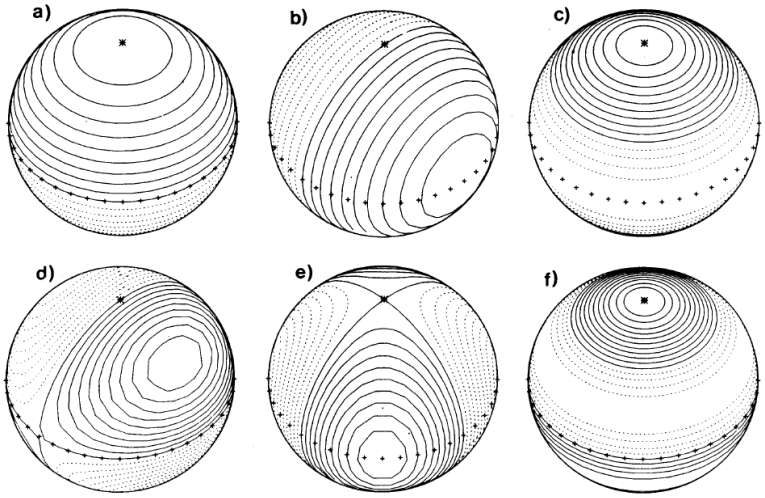

Figure 1.2: Contour plots of oscillations on the stellar surface for (a) $l = 1,\ m = 0$, (b) $l = 1,\ m = 1$, (c) $l = 2,\ m = 0$, (d) $l = 2,\ m = 1$, (e) $l = 2,\ m = 2$, and (f) $l = 3,\ m = 0$ pulsation modes. Solid lines indicate positive contours, and dashed lines indicate negative contours. The '+++' line marks the equator of the star. Different pulsation modes have different geometries. Reprinted from Christensen-Dalsgaard (2003).

Asteroseismology is the study of the radial and non-radial multi-periodic oscillations on stellar surfaces. From pulsations, we can often derive information regarding a star's internal properties and dynamics at the near-core regions. The more oscillation modes observed, the more information we can obtain (Shibahashi 2005). For instance, the single-period of Cepheid pulsations provides its mean density; meanwhile, the thousands of non-radial modes detected in our Sun have led to profound developments in helioseismology. Techniques and approaches adopted in asteroseismology largely originated from helioseismology, which were proven successful in deducing the physical conditions beneath the surface of our Sun (Christensen-Dalsgaard & Gough 1976). The study of solar oscillations has provided a substantial amount of information which probes the Sun's interior, such as the helium abundance and the differential rotation profile of the convective envelope (e.g. Gough 1983). Precise measurements of the solar core rotation rate have recently been achieved by de-

tecting the modulation of oscillation frequencies over two decades with SOHO data (Fossat et al. 2017). The modelling of solar rotation profiles is one of the major success in modern helioseismic research.

However, problems appeared when the techniques from helioseismology were applied to study other pulsating variable stars. These distant stars, compared to the Sun, have a significantly smaller apparent size such that it poses a challenge to map the surface velocities (Christensen-Dalsgaard 2003). The oscillation amplitudes are very small. In addition to the stars low apparent brightness, the observations suffer from high noise-levels (Pápics 2013). Furthermore, the pulsation periods of some non-radial stars are considerably longer than those of radial mode and ground-based observations can be limited due to daytime gaps. It was therefore necessary to develop high-resolution observing instruments, with continuous observations conducted over long timebases, such that the small-amplitude pulsation frequencies on stellar surfaces can be resolved and detected.

For this reason, the major advances in the field of asteroseismology have only been achieved in the recent years thanks to the development of high-resolution spectrographs and, in particular, space-based telescopes for carrying out continuous photometric surveys. Over the past few decades, the theoretical predictions and mathematical formulations of asteroseismology have been well-developed for constructing stellar models and simulating the pulsations. We are now entering the stage of verifying and constraining our theories with the high-precision observational data.

1.3 Theory of Stellar Oscillations

In Section 1.2, we described the surface pulsation geometry of non-radial variable stars. These oscillations can, in fact, be mathematically modelled as small perturbations superimposed on a star in an unperturbed state. By applying linear perturbation theory to the equations of hydrodynamics and assuming spherical symmetry, oscillations in pulsating stars can be modelled with spherical harmonic functions. We describe the displacement due to perturbations with a spherical coordinate system; radius r, co-latitude θ (measured from the rotation axis), and longitude ϕ. The displacement eigenfunctions are given by

$$\xi_r\ (r,\theta,\phi,t) = a_n\,(r)\ \ Y_l^m\ (\theta,\phi)\ e^{-i2\pi\nu t}, \tag{1.7}$$

$$\xi_\theta\ (r,\theta,\phi,t) = b_n\,(r)\,\frac{\partial Y_l^m(\theta,\phi)}{\partial\theta}e^{-i2\pi\nu t}, \tag{1.8}$$

$$\xi_\phi\ (r,\theta,\phi,t) = \frac{b_n\,(r)}{\sin\theta}\frac{\partial Y_l^m(\theta,\phi)}{\partial\phi}e^{-i2\pi\nu t}, \tag{1.9}$$

where ν is the pulsation eigenfrequency, $a_n\,(r)$ and $b_n\,(r)$ are the radial horizonal

displacement amplitudes, and $Y_l^m(\theta, \phi)$ are the spherical harmonics representing the angular dependence of the modes.We refer the interested reader to Christensen-Dalsgaard (2003) *Lecture Notes on Stellar Oscillations* for a complete derivation of the perturbation equations. These equations provide the mathematical basis for the three quantum numbers n, l and m which are illustrated in Figure 1.2. The spherical harmonic functions thereby set a constrain to the allowed values of m, ranging from $-l$ to l, hence the degeneracy is $(2l+1)$ modes per degree l. Non-radial oscillations have modes with $n > 0$ and $l > 0$; those with $l = 1$ are named dipole modes.

Under the assumption that radial order and degree are sufficiently large, we can apply the Cowling approximation (Cowling 1941) to neglect the perturbation in gravitational potential, and reduce the equations to second-order for simpler computation. The differential equation of the displacement wavefunction in the radial direction ξ_r can then be expressed in terms of acoustic frequency S_l and Brunt-Väisälä frequency N, giving

$$\frac{d^2\xi_r}{dr^2} = \frac{\omega^2}{c^2}\left(1 - \frac{N^2}{\omega^2}\right)\left(\frac{S_l^2}{\omega^2} - 1\right)\xi_r = -K(r)\xi_r, \tag{1.10}$$

(see e.g. Aerts et al. 2010, Christensen-Dalsgaard 2003). The characteristic frequencies S_l and N play important roles in determining the behaviour of oscillations. The wavefunction is oscillating with r when $K(r)$ is positive, and exponentially increasing/ decreasing when $K(r)$ is negative. In regions where the solution oscillates within a region and decays exponentially away from it, the solution is said to be trapped within an oscillation cavity. The boundaries of the trapping region are at points where $K(r) = 0$, i.e. the turning points of wave propagation in oscillations. The oscillating solutions thereby define the two major categories of pulsation modes: Pressure modes (p-modes), when $|\omega| > |N|$ and $|\omega| > S_l$; and Gravity modes (g-modes), when $|\omega| < |N|$ and $|\omega| < S_l$. Figure 1.3 illustrates the wave propagation in the stellar interior of p-modes and g-modes respectively.

The dominant restoring force of g-mode pulsations is gravitational force, which acts on the density perturbations from within the star. Gravity mode pulsations are driven by buoyancy force and can only propagate in radiative regions. Since g-modes are trapped within regions closer to stellar core, their oscillations carry more information on the physical conditions in the deep interior compared to p-modes. For high-order g-modes, assuming that the frequencies are low (i.e. $|\omega| \ll S_l^2$), it can be shown that the wavefunction becomes dominated by the spatial variation of N (see e.g. Christensen-Dalsgaard 2003). The propagation behaviour of g-modes is largely dependent on the Brunt-Väisälä frequency and mode trapping. Hence, g-mode pulsations play an important role in probing the near-core regions of γ Doradus variable stars.

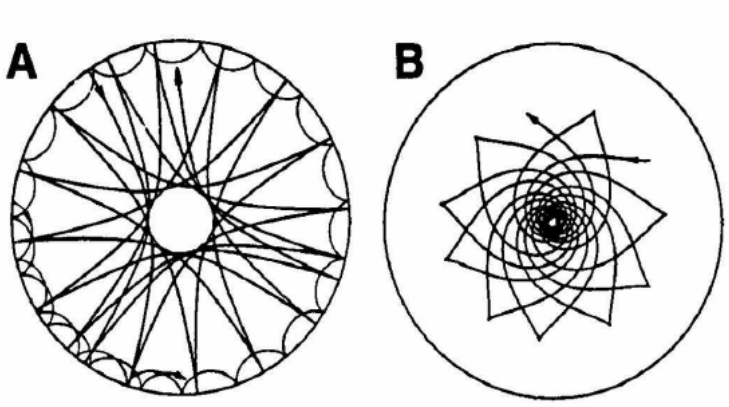

Figure 1.3: Ray paths of (a) two p-modes and (b) one g-mode in a solar model. The p-modes are trapped between an inner turning point and the surface, whereas g-modes are trapped within the deep interior close to the stellar core. Reprinted from Gough et al. (1996).

1.4 γ Doradus stars

γ Doradus stars (hereafter γ Dors) are late A- to early F-type stars which exhibit high-order low-degree non-radial g-mode pulsations (Kaye et al. 1999), with periods ranging from 0.3 to 3 days. They have typical masses of around 1.6 $M_{\odot}$ and radii ranging from 1.4 $R_{\odot}$ to 2.4 $R_{\odot}$ (Kaye et al. 1999), with temperatures of approximately 7200-7700 K at zero-age main sequence, and 6900-7500 K near the terminal-age main sequence (Handler 1999). γ Dor stars are located in the classical instability strip between solar-like stars and δ Scuti, close to the main sequence on the HR diagram, as illustrated in Figure 1.1. These stars are at the transition region between low-mass stars with convective envelopes and intermediate-mass stars with convective cores. This region is also where the CNO cycle becomes increasingly dominating relative to the pp-chain, causing the convective core to expand. The expansion then produces a chemical discontinuity at the edge of the fully-mixed core (Mitalas 1972, Silva Aguirre et al. 2011). The influence of chemical gradients on pulsations is further explained in Section 1.5.2.

The pulsation mechanism of γ Dor stars was first developed by Guzik et al. (2000) using the Frozen Convective (FC) assumption; that the oscillations are driven by the modulation of radiative flux by convection. The authors proposed that the FC mechanism is valid if the intermediate-mass stars have a sufficiently deep convective zone, such that the local convective timescale (i.e. time taken for a mass element to release excess heat to surroundings) at the base of convective zone is longer than the pulsation period. In this case, convection cannot instantaneously adapt to the changing conditions at base of the convective envelope during pulsation, leading to a modulation of radiative flux. Dupret et al. (2005a, 2007) further improved the driving mechanism theory by introducing the Time-Dependent Convection (TDC)

treatment (see e.g. Gabriel 1996, Grigahcène et al. 2005). TDC models have been proven successful in simulating the observed photometric amplitude ratios for γ Dor stars (Dupret et al. 2005a), thus becoming the current most widely-accepted theory for γ Dor pulsations.

The g-mode pulsations of γ Dor stars are driven by the physical processes at the base of convective zone from the deep interior. As a result, γ Dor oscillations predominantly trace the regions near the convective core boundary. These pulsating stars are therefore ideal and important for constraining the various stellar parameters, such as internal rotation profiles, chemical compositions, diffusive mixing and convective overshooting. By studying the pulsation period spacing pattern of γ Dor stars, we can characterize their interior properties and use the information to refine our theories of stellar structures and evolution.

Apart from gravity modes, oscillations in rotating γ Dor stars were recently found to exhibit gravito-inertial modes and Rossby modes, where the Coriolis force also acts as a restoring force for driving the pulsations (Antoci et al. 2019). It was first identified by Van Reeth et al. (2016) that Rossby mode pulsations could be present in many moderately- to rapidly-rotating γ Dor stars when fitting observed retrograde modes to theoretical models. Rossby waves (r-modes) originate from the coupling between toroidal motion and spheroidal motion caused by the Coriolis force (Papaloizou & Pringle 1978). This interaction drives perturbation in density and pressure of stars, hence the eigenfunctions and eigenfrequencies of r-modes may be treated in a similar manner as g-modes (Saio et al. 2018a). The same rotation formalism used in modelling g-mode pulsations can be applied to compute the mode visibility and estimate the expected frequency range of r-modes (Saio et al. 2018a).

Constraining the interior differential rotation profile of γ Dor stars is a challenge that asteroseismologists face. Rotation is known to have significant influence on stellar structure and evolution, however, its full impact is far from understood. The redistribution of angular momentum at different stellar ages remains one of the largest uncertainties in our evolution theories (e.g. Aerts et al. 2017, Ouazzani et al. 2019, Dupret 2018). In order to describe differential rotation, we apply the same rotation formalism used for rigidly-rotating stars, and generalize the pulsation equations such that the eigenvalue is a function of the radial component r (Van Reeth et al. 2018). The mathematical relation between pulsation periods and the rotation profiles is thus established. Characterization of near-core internal rotation profiles is crucial to explain the large drop in rotation rate when the star evolves from the core hydrogen burning to core helium burning stage (Aerts et al. 2017). Theories for describing rotation effects are applied to observed phenomena in stellar pulsations, such as period spacings, in order to determine the rotation rate of the near-core regions. It is therefore important to ensure that the fundamental formalisms and modelling methods adopted in our current research are sufficiently accurate.

1.5 Period Spacings of pulsations

The spacings between pulsation periods are highly sensitive to the inner properties of the star. The variation of period spacings with respect to period can act as an asteroseismic diagnostic by providing information such as the rotation rate and the convective core overshooting. Tassoul (1980) showed that for non-rotating stars with an inner convective core and outer radiative envelope, the first-order asymptotic approximation of pulsation period spacings for high-order low-degree g-modes is given by

$$\Delta P_{nl,asymp} = P_{n+1,l} - P_{nl} = \frac{2\pi^2}{\sqrt{l(l+1}} \left(\int_{R_{cc}}^{R_*} \frac{N(r)}{r} dr \right)^{-1} = \frac{\Pi_0}{\sqrt{l(l+1)}}, \qquad (1.11)$$

where $P_{n,l}$ and $P_{n+1,l}$ are the periods of two consecutive radial order modes with the same degree l. R_* and R_{cc} indicate the radius of the star and the convective core, which are the turning points of the mode oscillation cavity. The period spacing is expected to be constant for a single non-rotating stellar model. The spatial integral of Brunt-Väisälä frequency $N(r)$ in Equation 1.11 also shows that the value of the asymptotic period spacing is dependent on the size of the core, whereas the structure of period spacings are related to mixing processes in the radiative envelope above the convective core (Miglio et al. 2008). Π_0 is a parameter which includes the integral term and it represents the asymptotic period spacing without the l-dependency, hence $\Delta P_{nl,asymp}$ is often written as $\Delta \Pi_l$.

The following sections illustrate how the period spacing pattern of g-mode pulsations is affected by stellar age, convective core overshooting, and stellar rotation.

1.5.1 Effect of Stellar age

As the star evolves during main-sequence phase, the shrinking core increases the stellar density and pressure. This causes $N(r)$ and the integrand in Equation 1.11 to increase (Moravveji et al. 2015), leading to a decreasing period spacing. Figure 1.4 shows the change in asymptotic period spacing of an example stellar model as it evolves from zero-age main sequence (ZAMS) to terminal-age main sequence (TAMS). The decreasing X_c denotes the evolution timestep. This agrees with the literature (e.g. Schmid & Aerts 2016, Moravveji et al. 2015).

1.5.2 Effect of Convective core overshooting

Pulsations of g-modes are highly sensitive to the mixing process near the convective core. As the core shrinks during main-sequence evolution, the central hydrogen content decreases and leaves behind a chemical composition gradient of burnt material at the convective core boundary (Moravveji et al. 2015). Equation 1.11 shows that

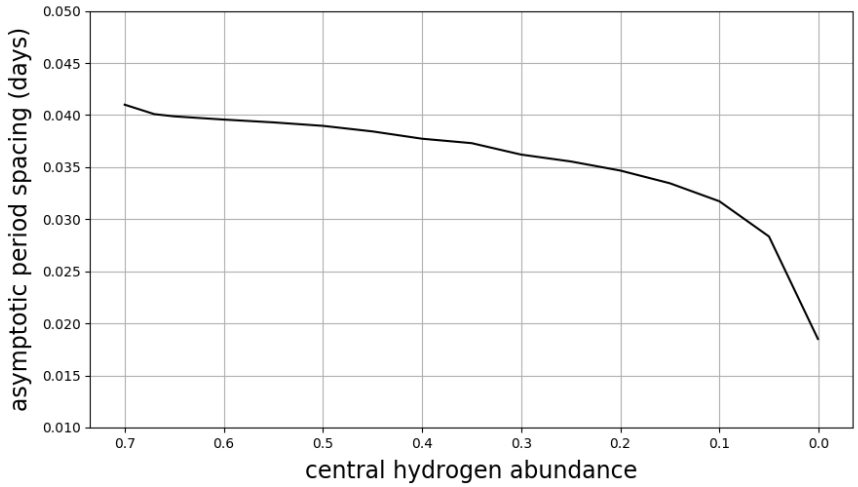

Figure 1.4: Evolution of asymptotic period spacing as a function of central hydrogen abundance X_c, computed with a MESA stellar model of mass 1.0 $M_\odot$ simulating a non-rotating γ Dor star. The asymptotic period spacing decreases as the star evolves from ZAMS to TAMS, and the rate of decrease rises significantly towards the end of its main-sequence phase.

the propagation of g-modes is dependent on the Brunt-Väisälä frequency. Assuming ideal gas law applies, the expression of frequency N can be approximated as

$$N^2 \simeq \frac{g^2\rho}{p}(\nabla_{ad} - \nabla + \nabla_\mu) \quad , \tag{1.12}$$

where ∇_μ is the gradient of chemical composition, and has a positive contribution to frequency N. Therefore, steep gradients in hydrogen abundance created during evolution will cause sharp features (or spikes) to appear in the spatial variation of Brunt-Väisälä frequency (Miglio et al. 2008).

From Equation 1.10 we know that the frequency N is related to the turning points of wave propagation. Sharp features in N could lead to a resonance conditions which contributes to mode trapping in the stellar interior (Brassard et al. 1991). Both horizontal and radial components of the eigenfunction are partly trapped in the region where the sharp feature of N is located, and this hence impacts the pulsation periods of the star (see e.g. Fig. 3 in Miglio et al. 2008).

Derivations presented by Miglio et al. (2008) show that sharp features in N will introduce a sinusoidal component into the oscillations periods expression (Equation 1.11), and therefore lead to deviations from the uniform period spacings predicted

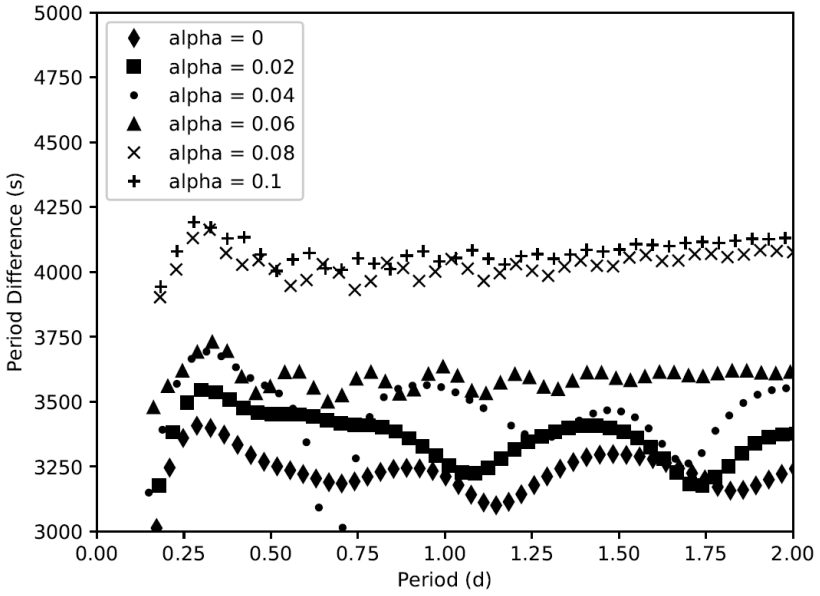

Figure 1.5: Period spacing patterns of a non-rotating 1.6 $M_{\odot}$ model with the convective core overshoot parameter f_{ov} varying from 0.0 to 0.1 in steps of 0.02. The period spacing pattern exhibits sinusoidal behaviour when no overshoot is added. The curve becomes increasingly flat as overshoot increases and smooths out the chemical discontinuities. The average period spacing of the pattern also increases with core overshooting. Reprinted from Lovekin et al. (2017).

by Tassoul (1980). This component is seen as dips in the period spacings of g-modes. The amplitude of this sinusoidal component is dependent on the sharpness of the N distribution (Miglio et al. 2008). Therefore, by looking at the depth and regularity of the dips in a period spacing pattern, we can indicate the steepness and location of the chemical discontinuity, and deduce information about the convective core.

By adding core overshooting, chemical discontinuities are 'washed out' due to mixing effects and the prominence of dips in the period spacing pattern is reduced (Van Reeth et al. 2015). This effect is shown in Figure 1.5. Furthermore, from the integration limits in Equation 1.11 we know that the asymptotic period spacing is dependent on the size of the fully mixed core (Moravveji et al. 2015). Convective overshoot effectively increases the core radius, and hence the integral term decreases, causing the period spacing to rise. Such trend is identical to that produced by increasing stellar mass (Lovekin et al. 2017), which shows that convective core overshooting is also effectively increasing the mass of the stellar core.

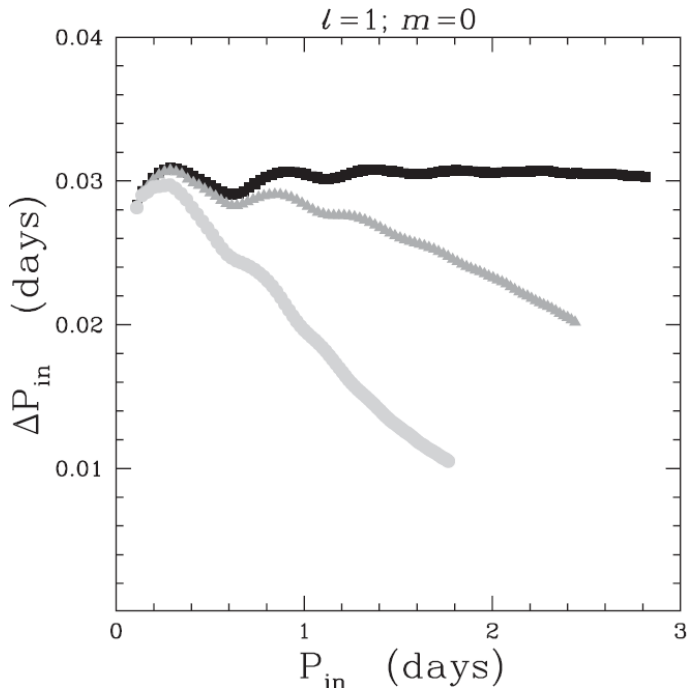

Figure 1.6: Period spacing pattern of a (1,0) g-mode pulsation in inertial frame with an increasing rotation rate (black to light grey). This model has turbulent diffusion $D_t = 100$ cm^2 s^{-1} which introduces chemical mixings in the star and smooths out the period spacing curve. At zero rotation, the curve appears horizontal with several dips at short periods. Stellar rotation causes the zonal mode period spacings to decrease with period, with a gradient that is proportional to its rotation rate. Curves with more rapid rotation appear smoother compared to those with no rotation. Reprinted from Bouabid et al. (2013).

1.5.3 Effect of Rotation

Stellar rotation causes the oscillation frequencies to deviate from equal spacing and has two major effects on the period spacing pattern: **i**) The gradient of the period spacing pattern is uniquely correlated to the rotation rate (Ouazzani et al. 2017). For periods measured in the inertial frame, the slope increases for prograde modes, and decreases for both zonal and retrograde modes (Bouabid et al. 2013). **ii**) Chemical discontinuities around the convective core cause the period spacings to oscillate, seen as dips in the spacing pattern (Miglio et al. 2008). The periodicity of the dips is related to the location of the chemical gradient. Since rotation also induces mixing processes at the core boundary, it reduces the amplitude of the dips and alters the dip locations. Figure 1.6 illustrates a typical period spacing pattern of a stellar model rotating in zonal mode (1,0) with increasing rotation rates.

Table 1.1 summarizes the major influence of stellar age, convective core overshoot-

Table 1.1: Summary of Section 1.5 on the different ways the pulsation period spacing pattern can reflect the internal properties of the γ Dor star.

Stellar properties	Effect on Period Spacing pattern
Stellar Age	• Decreases the average period spacings as star evolves from ZAMS to TAMS at an increasing rate
Convective core overshooting	• Smooths out the dips in the period spacing; Increases the average period spacing of the curve
Interior Rotation	• Introduces a slope to the curve, which increases for prograde modes, and decreases for zonal and retrograde modes in the inertial frame • The gradient is directly proportional to the rotation rate • Smooths out the dips in the period spacings as rotation rate increases

ing and rotation on the period spacing curve of γ Dor pulsations. Period spacing patterns are also highly sensitive to other stellar parameters such as mass, diffusive mixing and chemical compositions. We make use of these observable characteristics in the oscillation frequencies to derive and constrain the physics of the stellar interior.

1.6 Rotation Formalisms

Rotation of a star induces Coriolis and centrifugal forces which distort the equilibrium structure and the oscillation cavity of gravity modes (Ballot et al. 2010). These inertial forces modify the set of oscillation differential equations, and thereby the spectrum of eigenfrequencies (Lee 2013). Since rotation breaks the spherical symmetry, pulsations are no longer described by single spherical harmonics and the eigenvalue problem has to be solved in 2-D in order to treat higher rotation rates. The Two-dimensional Oscillation Program (TOP) developed by Reese et al. (2006) is an example of a 'complete calculation' which produces highly accurate results for the pulsation frequencies for arbitrarily rapid rotations. These 2-D codes are often used for verifying other rotation formalisms.

We are currently capable of computing the 2-D 'complete' impact of rotation. However, such methods are computationally expensive (Ballot et al. 2010), and difficult to be employed in detailed ensemble modelling for the large amount of observational data (Mathis & Prat 2019). We often make use of various approximations within certain rotation limits to simplify the mathematics into 1-D pulsation equations. In the following section, we present the common rotation formalisms adopted in previous studies for modelling γ Dor stars and discuss their domains of validity.

1.6.1 Perturbative Approach

For perturbative methods, the effect of rotation is treated as a small perturbation to the oscillation equations such that the 2-D problem is transformed into a sequence of 1-D problems. In a kth-order approach, the pulsation frequencies in the co-rotating frame ω_{nlm}^{pert} are developed as a function of rotation rate Ω, given by

$$\omega_{nlm}^{pert} = \omega_{nl}^{0} + \sum_{j=1}^{k} C_{nlm}^{j} \Omega^{j} + O\left(\Omega^{k+1}\right), \tag{1.13}$$

where ω_{nl}^{0} is the frequency for non-rotating case, Ω is the rotation frequency, and C_{nlm}^{j} are the perturbation coefficients. $O\left(\Omega^{k+1}\right)$ is a residual term which contains all expansion terms beyond the k-th order; this parameter is assumed to be very small relative to the $j = 1 \ldots k$-th terms and it is neglected in the calculations. The perturbation coefficients are constants that can be numerically calculated by fitting the oscillation results. Equation 1.13 can be rewritten to explicitly express the m-dependence of each perturbative coefficient obtained from theoretical derivations, giving

$$\omega_{nlm}^{pert} = \omega_{nl}^{0} + mC_{ln}\Omega + \left(S_{ln}^{1} + m^{2}S_{lm}^{2}\right)\Omega^{2} + m\left(T_{ln}^{1} + m^{2}T_{lm}^{2}\right) + O\left(\Omega^{4}\right), \tag{1.14}$$

(see e.g. Ballot et al. 2010, Lee 2013). The first-order correction term is proposed by Ledoux (1949) and describes the effect of Coriolis force, which is different for prograde and retrograde modes as indicated by the factor of m. The second-order is proposed by Saio (1981) and it takes both Coriolis and centrifugal force into account. The third-order term further considers the coupling between non-spherical symmetry distortion and the Coriolis force, as well as the near-degeneracy of modes (Soufi et al. 1998). As the rotation rate Ω increase, the influences of centrifugal and Coriolis forces become increasingly significant, and hence higher-order correction terms are required to describe the rapidly-rotating stars.

Studies presented by Ballot et al. (2010) outlined the domains of validity of the first, second and third-order perturbative approach by comparing the frequencies computed with perturbative methods to those obtained from 2-D 'complete calculations'. The result for $l = 1$ modes of γ Dor stars is shown in Figure 1.7. The second-order calculation gives satisfactory results for stars with rotation rates up to $\Omega/\Omega_k = 0.3$, where $\Omega_k = \sqrt{GM/R^3}$ is the critical (break-up) rotation rate of the star. The third-order calculation further extends the domain of validity to approximately $\Omega/\Omega_k = 0.4$. These results indicate that the second-order correction gives a reasonable description of the centrifugal distortion, but perturbative methods are unable to give accurate results in the low-frequency regime where $\omega < 2\Omega$ as marked by the purple line in Figure 1.7. This shows that perturbative methods are unable to take into account changes in the shape of the mode cavity. The perturbative approach is only valid when the star's rotation is sufficiently slow such that $\Omega \ll \omega$ and $\Omega \ll \Omega_k$ (Ballot et al. 2013). Note that the stellar models used in the above

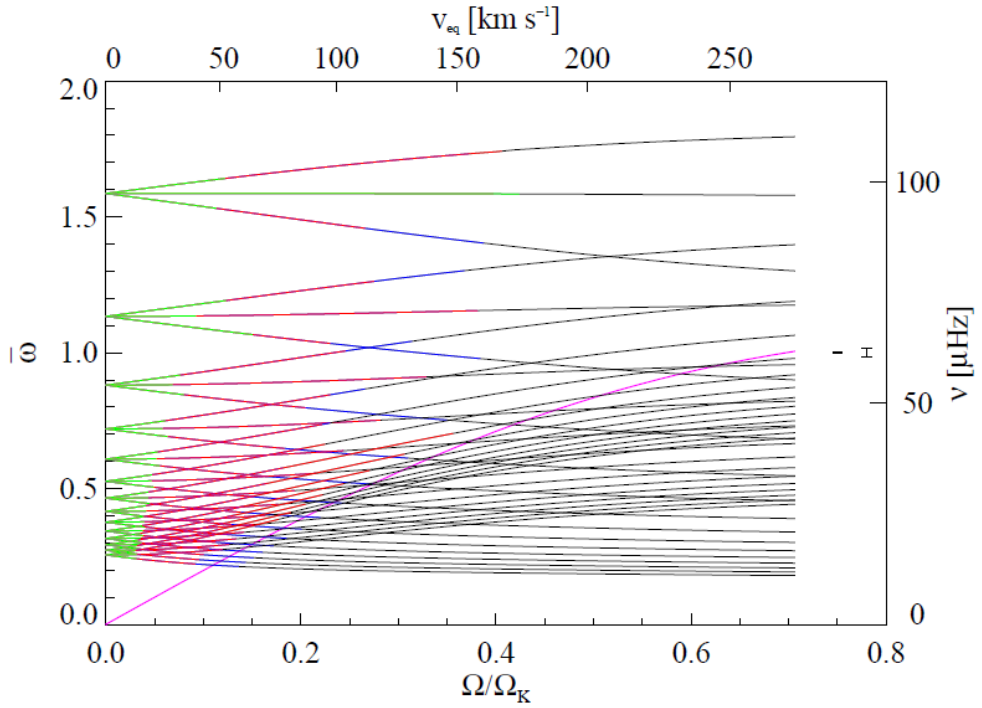

Figure 1.7: Pulsation frequencies of an $l = 1$ mode of γ Dor star from complete calculations plotted against rotation rate. Green/red/blue parts of the curve indicate regions where the frequencies from first/second/third-order approach match the complete calculations. The domain of validity extends towards higher rotation rates as the order increases. The purple curve indicates the boundary equation $\omega = 2\Omega$ below which none of the perturbative methods are valid. Reprinted from Ballot et al. (2010).

analysis are polytrope models, where the Equation of State is described by a proportionality between pressure and density in the stellar interior. The results may differ to those computed with realistic stellar models adopted in this work.

In this thesis, we focus on using the Second-order Perturbative method to model γ Dor stars. Following the method adopted by Gough & Thompson (1990), the effect of rotation on the pulsation frequency ω_{nlm} of a star with uniform rotation rate Ω in inertial frame can be written in the form

$$\omega_{nlm}^{pert} = \omega_{nl}^{0} + \omega_1 + \left(\frac{\Omega^2}{\omega_{nl}}\right)\left(\Delta_{nl}^{(1)} + m^2\Delta_{nl}^{(2)}\right) + \left(\frac{\Omega^2 R^3}{GM}\right)\omega_{nl}\Delta_{nl}^{(3)}Q_{2lm}, \qquad (1.15)$$

(see Burke et al. 2006, Kjeldsen et al. 1998). $\Delta_{nl}^{(1)}$ is the m-independent second-order perturbation term which originates from the toroidal perturbation due to Coriolis forces, $\Delta_{nl}^{(2)}$ is similar to $\Delta_{nl}^{(1)}$ but for the m^2-dependent terms, and $\Delta_{nl}^{(3)}$ takes the

effect of centrifugal distortion into account. The Q_{2lm} in last term of Equation 1.15 is defined as

$$Q_{2lm} = \frac{\int_{-1}^{1} P_2(x)[P_l^m(x)]^2 dx}{\int_{-1}^{1}[P_l^m(x)]^2 dx} \tag{1.16}$$

(see e.g. Burke et al. 2006, Kjeldsen et al. 1998, Gough & Thompson 1990), where $P_2(x)$ is the Legendre polynomial of $n = 2$, and $P_l^m(x)$ are the associated Legendre polynomials. Equation 1.16 can be further approximated as $Q_{2lm} \simeq -\frac{1}{2}P_2\left(\frac{m}{L}\right)$ for $l \gtrsim 2$ (Kjeldsen et al. 1998). The second term of Equation 1.15 is the first-order perturbation of oscillation frequency, namely, the rotational splitting observed in slowly rotating stars. It is given by

$$\omega_1 = m\beta_{nl}\int_0^R K_{nl}(x)\Omega(x)dx \tag{1.17}$$

(see e.g. Kurtz et al. 2014, Christensen-Dalsgaard 2003), where x is the radial coordinate of the star. Under the influence of the Coriolis force, the unperturbed pulsation frequency splits into $(2l+1)$ multiplets which correspond to each value of azimuthal order m. The integral in Equation 1.17 gives the rotation rate averaged with respect to the oscillation displacement eigenfunctions of an eigenmode with order n and degree l (Unno et al. 1989, Aerts et al. 2010). Beta β_{nl} and the rotational kernel K_{nl} are mathematical expressions which involve the integration of the eigenfunctions and the density of the ideal gas star over the stellar radius (e.g. Kurtz et al. 2014). The rotational kernel thus represents the sensitivity of frequency splitting to the rotation rate of the star (García et al. 2019).

Figure 1.8 shows the effects of frequency shifts and rotational splitting caused by each perturbation term in Equation 1.15. Term (0) is the frequency for a non-rotating case of the same stellar model. Term (1) is not included in Equation 1.15 but it is often employed to describe the change in mean radius and sound speed due to fast rotation (Kjeldsen et al. 1998). (2) is the β_{nl} term from Equation 1.17; (3) is the $\Delta_{nl}^{(1)}$-term; (4) the $\Delta_{nl}^{(2)}$-term; and (5) the $\Delta_{nl}^{(3)}$ and Q_{2lm}-terms from Equation 1.16. A final set of oscillation frequencies is obtained after taking all of the above terms into account. To compute the frequencies for a particular oscillation mode, we extract the final frequencies of those corresponding to the same azimuthal order m. These frequencies are described in the inertial frame of reference (i.e. in an observer's point of view).

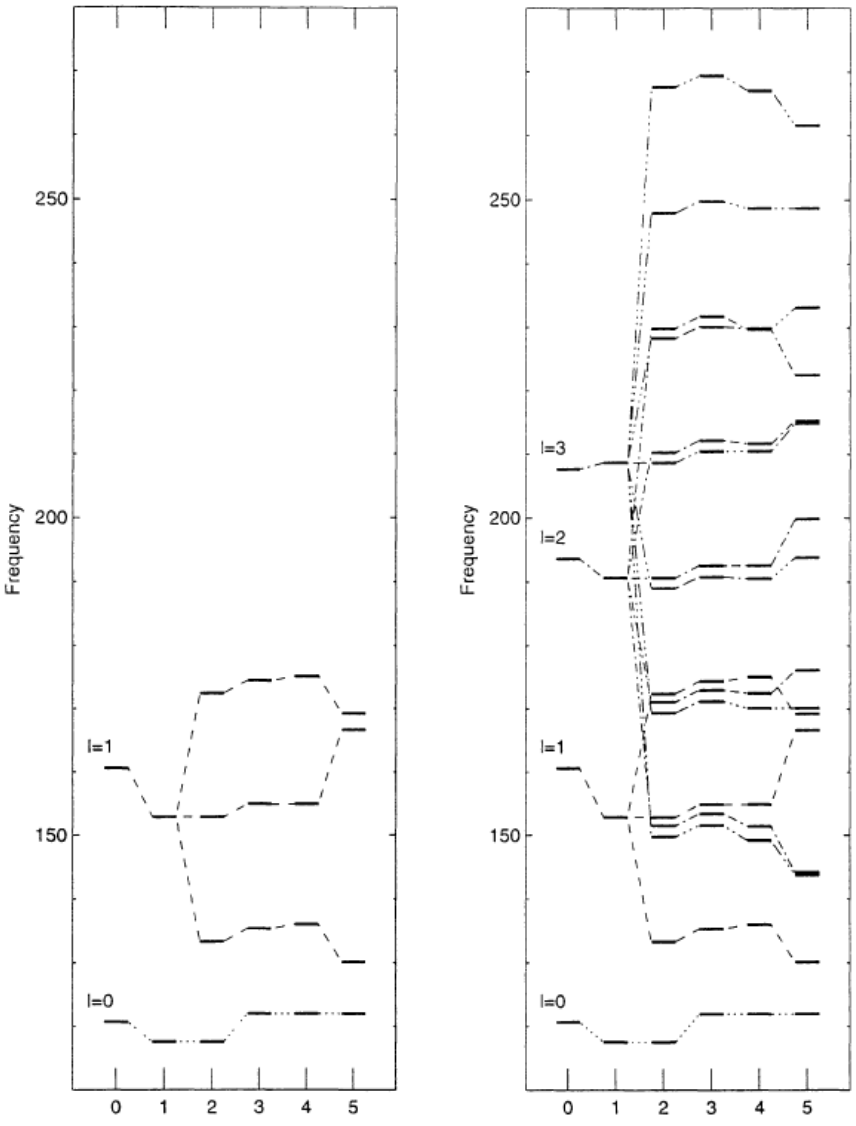

Figure 1.8: Illustration of rotational splitting effects on the oscillation frequencies for an example model with radial order $n = 1$. The horizontal axis corresponds to the contributions of each perturbation term in Equation 1.15. Term (0) indicates the non-rotating case; (1) shows the effects of change in model structure; and (2) to (5) are the terms in Equation 1.15. Term (2) splits the frequencies into multiplets while the rest of the terms shift the frequencies. (5) gives the final set of pulsation frequencies after taking all terms into account; the spacings between the frequencies are non-linear. The left-hand panel shows results for $l = 0$ and $l = 1$ modes for clarity, and the right-hand panel also includes those for $l = 2$ and $l = 3$ modes. Reprinted from Kjeldsen et al. (1998).

1.6.2 Traditional Approximation of Rotation

For low-frequency oscillations with a moderate rotation rate of $|\Omega/\omega| \gtrsim 1$, non-perturbative methods are required. Traditional Approximation of Rotation (TAR; Eckart 1960) is a treatment of rotation effects which leads to a simplification of the pulsation equations. First, the rotation is assumed to be uniform. Next, TAR neglects the centrifugal distortion by assuming $\Omega \ll \Omega_k$ to maintain spherical symmetry in the star's shape. The Cowling approximation is then applied to neglect the perturbation of gravitational potential (Cowling 1941). Considering the properties of high-order low-frequency g-modes, we also assume that the buoyancy force is stronger than the Coriolis acceleration (i.e. $2\Omega \ll N$) in the direction of chemical stratification, such that the horizontal component of the Coriolis force can be neglected (Mathis & Prat 2019). The above assumptions allow the pulsation equations to become separable (Townsend 2003a). The solution to this equation proceeds just like the non-rotating case with only two major changes: **i**) The dependence of the eigenfunction (spherical harmonics) is replaced by Hough functions which are eigensolutions of Laplace's tidal equation,

$$L_\nu \left[\Theta^m_{l\nu}(\mu)\right] = -\lambda \Theta^m_{l\nu}(\mu) \tag{1.18}$$

(see e.g. Lee & Saio 1997, Townsend 2003a, Bouabid et al. 2013); and **ii**) The $l(l+1)$ eigenvalue term is replaced with $\lambda_{lm\nu(n)} = \widetilde{l}\left(\widetilde{l}+1\right)$ where $\widetilde{l}$ is the effective harmonic degree introduced by Townsend (2000). The Hough function consists of a spin parameter ν associated with each solution to the eigenfunction, defined by

$$\nu = \frac{2\Omega}{\omega_{co}} \tag{1.19}$$

(see e.g. Lee & Saio 1997), where ω_{co} is the pulsation frequency in the co-rotating frame. The spin parameter can be thought as a measure of the extent a mode is 'aware' that its frame is rotating (Townsend 2013). The eigenvalues $\lambda_{lm\nu(n)}$ vary as a function of spin parameter for both prograde and retrograde modes (see e.g. Fig. 1.8 in Van Reeth 2017), and therefore it is dependent on the stellar rotation rate Ω as described in Equation 1.19.

We can thereby replace the term $l(l+1)$ in Equation 1.11 and rewrite the pulsation period series expression $P_{co}(n)$ within TAR in the co-rotating frame as

$$P_{co}(n) \simeq \frac{\pi^2}{\sqrt{\lambda_{lm\nu(n)}}} \left(\int_{R_{cc}}^{R_*} \frac{N(r)}{r} dr\right)^{-1} (2n+1) \tag{1.20}$$

(see e.g. Bouabid et al. 2013). Since the eigenvalue λ varies with spin parameter ν, which is dependent on rotation Ω, the relationship between period $P_{co}(n)$ and

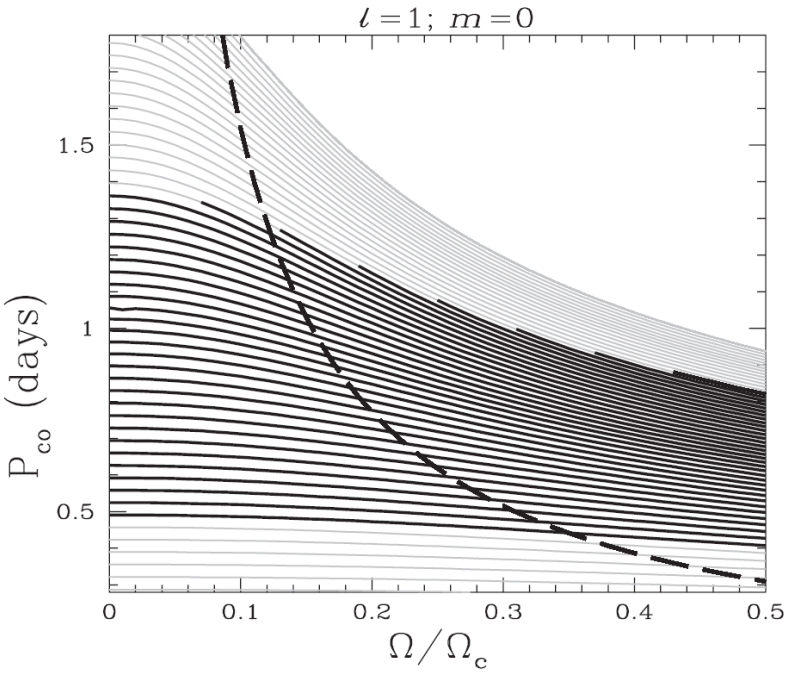

Figure 1.9: Change in pulsation periods in the inertial frame as a function of the rotation frequency ratio for an example stellar model with pulsation mode (1,0). Each curve represents the frequency of a radial order n. Thin lines indicate that the mode is stable, and thick lines indicate unstable modes. The curves have equal spacings at zero rotation, but those with longer periods become increasingly dense as rotation is increased. The dashed line represents the limit of the inertial regime. Note that Ω/Ω_c on the horizontal axis is equivalent to Ω/Ω_k. Reprinted from Bouabid et al. (2013).

rotation frequency can be deduced. We can then transform the TAR pulsation periods in the co-rotating frame to the inertial frame using the relation

$$P_{in} = \frac{1}{1/P_{co} + m f_{rot}} \tag{1.21}$$

(see e.g. Li et al. 2019c), where P_{in} is the period in inertial frame and f_{rot} is the rotation frequency of the star. Figure 1.9 plots the relation between the TAR asymptotic pulsation periods defined in Equation 1.20 in the inertial frame, and the rotation frequency ratio Ω/Ω_k. It can be seen that at zero rotation rate, the period curves are equally spaced as predicted in the asymptotic expression in Equation 1.11. As the rotation rate increase, the spacings between each curve at longer periods become increasing smaller. This justifies the negative slope in the period spacing pattern shown in Figure 1.6, and indicates that the gradient of the slope increases with rotation.

TAR is one of the most common formalisms adopted for modelling the rotation of γ Dor stars. Previous work has shown that this formalism is sufficiently accurate for deriving the interior rotation rates of γ Dor stars from observed pulsation data (see e.g. Van Reeth et al. 2016). However, because TAR is formulated based on the assumptions that $\Omega \ll \Omega_k$ and $2\Omega \ll N$, the deformation effects from centrifugal force in rapidly rotating stars are not considered; this thereby defines the upper limit of its domain of validity. Yet, Mathis & Prat (2019) have recently shown that TAR can be mathematically generalized to include the effects of rotational deformation for a spheroidal star, given that the rotation rate satisfies the condition $2\Omega \ll N$. This result shows that the domain of validity of TAR can potentially be extended.

1.6.3 Other non-perturbative approaches

Other non-perturbative formalisms are also employed to model stars with rotation rates beyond the limit of TAR. For example, the ray-tracing method describes the propagation of waves with ray dynamics analogous to geometrical optics. It modifies TAR by taking the full Coriolis acceleration into account without neglecting any components, and computes the oscillation modes by considering the wave interference (Prat et al. 2016). The series expansion method is another formalism which describes the rotational deformation of structure in stars with very rapid rotation, where new coordinate systems are introduced to reformulate the pulsation equations (Lee 2013). Both of these approaches are beyond the scope of the work treated in this thesis.

1.6.4 Limitations of 1-D rotation modelling

Stellar rotation modelling in 1-D requires simplifications to mimic the 2-D, or even 3-D, mixing effects in the deep interior due to rotation. The perturbative method and TAR formalisms themselves do not compute the mixings, but instead they provide approximations to describe their observable effects on the pulsations. The codes use the model's Brunt-Väisälä frequency distribution to estimate the chemical discontinuities around the core, and simulate the dips (i.e. the sinusoidal components) in the period spacing curve which are directly associated with the interior mixing. Because these computations are independent of a dynamic stellar model, their rotational mixing treatments are unable to take further stellar processes into account and they are thus intrinsically limited. For instance, the origin of dips observed in real stellar pulsations also involves mode coupling, yet such effects are not considered in TAR (Dupret 2018, Saio et al. 2018a). This shows that the simulation of observable rotational mixing effects can vary across different formalisms.

1.7 Research Goals of this Thesis

Rotation formalisms have been widely used for modelling the observed pulsation period spacing patterns and constraining the interior rotation rates through optimization. The perturbative approach describes the effects on pulsations caused by slow rotation, and TAR describes those for moderate rotation. The rotation rate which we derive from fitting observational data is dependent on our chosen formalism. Yet, without knowing the rotation rate prior to choosing an appropriate theoretical framework, we cannot decide on which formalism to adopt. For example, γ Dor stars have pulsation frequencies similar to the rotation frequency; both perturbative methods and TAR are hence valid modelling methods within different ranges relevant to these stars.

This research aims to develop a method which allows us to determine the most suitable formalism for any given set of observed frequency data. This method must be solely based on the analysis of period spacings, which is currently our only means of deriving the interior rotation rate We investigate how the different rotation formalisms are distinguishable in g-mode period spacings such that they can be compared to observed data. This thesis also analyses the correlations between parameters in modelled pulsation period series. It was recently found that SPB stars reveals correlations amongst the parameters for models within a localized parameter space (Pedersen et al. 2018). For this reason, we investigate if such correlations are seen in the g-mode pulsations of γ Dor stars.

The research method outlined in this thesis is applicable to all different kinds of theoretical inputs available in seismic modelling. Despite the success of current models allowing precise determination of rotation profiles, these theories are possibly no longer valid for other stellar processes such as the evolution of interior angular momentum distribution (e.g. Aerts et al. 2017). Ouazzani et al. (2019) used the near-core rotation rates of γ Dor samples, derived from observed period spacings with TAR, to confront the models of angular momentum transport evolution in intermediate-mass stars. It was found that the measured rotation rates do not fall within their expected intervals, which are hypothesized based on angular momentum transport theory of Maeder & Zahn (1998). The conflict between the two theories is an indication of, either, our description of the angular momentum transport mechanism is incomplete, or, TAR is not sufficiently accurate for modelling rotation rates.

Hence, refining the existing stellar rotation formalisms remains a major challenge in modern asteroseismic research. As new space missions such as TESS deliver more high-precision data, we are gaining large numbers of detected modes from each pulsating star. These data act as constraints for verifying the reliability of our stellar theories. It is thus important to develop accurate modelling methods in order to correctly interpret the data with the lowest computational cost.

Chapter 2

Methods

The large number of pulsation frequencies detected from space-based observations have provided us the opportunity to model γ Dor stars with non-uniform period spacings. Guided by theoretical predictions on the structure and oscillations of these stars, seismic modelling methods were developed and applied to observations to determine their stellar properties (e.g. Li et al. 2019c, Van Reeth et al. 2016, Schmid et al. 2016 and references therein). Asteroseismologists scan over grids of models with varying parameters and compute a set of pulsation frequencies for each model. The grids are then compared against the data for a target γ Dor star through χ^2 minimization to obtain the best-fit model.

In this chapter, we present our methodology to examine the reliability of our state-of-the-art modelling techniques. Instead of using real pulsation data, we use the oscillation frequencies computed from benchmark models as modelling targets, with the advantage of having known stellar parameters, as opposed to those from real stars. This method was used by Pedersen et al. (2018) and Mombarg et al. (2019) for comparing theoretical models with different overshooting prescriptions. We used the stellar evolution code MESA and the oscillation codes ADIPLS and GYRE to simulate the pulsation period series of γ Dor stars. The gradient and the intercept of the benchmark models were then used as test conditions to extract the best-matching models from the grids.

2.1 MESA stellar evolution code

Modules for Experiments in Stellar Astrophysics (MESA, v10398; Paxton et al. 2011, 2013, 2015, 2018) is an open-source 1-D stellar evolution code used for creating stellar models and computing the various stellar properties as the star evolves. The code consists of a wide range of modules which solve the fully-coupled stellar structure equations and chemical composition equations simultaneously (Paxton et

al. 2011). The modules in MESA provide the Equation of State, opacity tables for the chemical elements, nuclear reaction rates and diffusion data, allowing the user to simulate the evolution of stars with customized settings. MESA allows users to set the initial conditions and choose stellar theories to be employed in the model through the inlists, which are input files containing all user-defined parameter values and choices of theorical descriptions. MESA also provides 'hooks' where the user can incorporate their own codes to the computation without editing the core algorithms, such as coupling MESA to other stellar pulsation codes. Hence, MESA is a useful tool for testing newly developed theories and computational codes.

To begin a simulation, MESA requires the input of the model's initial conditions. This includes the stellar mass, convective core overshoot parameter, diffusive mixing parameter and chemical composition. A variety of pre-computed opacity tables and nuclear reaction networks are available in MESA, where the user can specify their options in the inlist. We start by loading a default pre-main-sequence model, then run the code to simulate the evolution of the star by solving the structure equations and equations of state at every evolutionary timestep. At each timestep, MESA outputs a model containing the stellar parameters at every mesh point along the radius. The code uses an adaptative mesh and timestep refinement to control the size of steps, allowing details in the change in properties of the stellar interior to be revealed. The model evolves until the stellar parameter(s) reaches the stopping condition defined by the user, such as setting limits to the abundances of chemical elements in the stellar core.

MESA is used in this work for creating stellar models which simulate γ Dor stars, with varying parameters including initial mass, stellar age, and convective core overshooting. We took the MESA Summer School teaching material[1] (2016) produced by Prof. Conny Aerts as reference to setup the other MESA inputs, such as the chemical abundances and the diffusive mixings. The initial chemical compositions of these models are fixed at a metallicity of $Z = 0.02$ and a helium abundance of $Y = 0.28$. We adopted the OPAL type 1 opacity tables (Rogers & Nayfonov 2002) based on the solar metallicity table from Asplund et al. (2009). We used the central hydrogen abundance X_c as an indicator of stellar age, which decreases from 0.69 at ZAMS to 0.001 at TAMS during the star's main-sequence phase. In order to end the simulation precisely at the specified abundance, we ensure that the step in X_c between evolutionary modes is sufficiently small by setting the maximum allowed timestep to 10^7 years. Additional mesh controls were also employed to resolve the g-modes near the convective core boundaries. We increased the resolution in regions where the chemical gradients of helium are large around the hydrogen core. These are the core settings required for creating γ Dor models and remained unchanged.

Convection in the 1-D MESA code is treated with the Mixing Length Theory (Sec-

[1]MESA marketplace http://cococubed.asu.edu/mesa_market/

tion 1.1). We used the Henyey description of mixing effects and fixed the parameter α_{MLT} at 1.8. We applied the Ledoux criterion for a stable radiative layer, and the semi-convection efficiency parameter α_{SC} was fixed at 0.01. Convective core overshooting is modelled by taking the diffusion mixing coefficient at the convective boundary r_{cc}, and extending it for a distance defined by $f_{ov}H_P$, where f_{ov} is the overshooting parameter. However, because the mixing coefficient at the exact edge is zero, we take the mixing coefficient at stellar radius $r_0 = r_{cc} - f_0 H_P$ inside the core as the 'starting point' of overshoot, where f_0 parameterizes the distance to the core boundary (Paxton et al. 2011, Pedersen et al. 2018). We employed the exponential overshooting description, which assumes the mixing effects to decay exponentially with the radius of the star. An extra constant diffusive mixing of 1.0 was also added beyond the overshooting range in the radiative envelope, which influences the shape of the chemical gradient at the core boundaries. The parameter f_0 was fixed at 0.005 and we varied the parameter f_{ov} to control the amount of overshooting from the convective core boundary. An example of the MESA inlist set-up is provided in Appendix A.

Whilst MESA provides modules to add rotational effects to the stellar model, it was shown that the treatment of rotational mixing effects is badly constrained in 1-D computational codes (e.g. Van Reeth 2017). For this reason, we only considered non-rotating models in MESA, and we add in the rotational effects when the stellar model is being exported to the pulsation codes, GYRE and ADIPLS, for computing the oscillation frequencies.

2.2 GYRE oscillation code

GYRE (v5.1; Townsend & Teitler 2013, Townsend et al. 2018) is an open-source 1-D stellar pulsation code which is incorporated in the MESA astero module. With an input equilibrium stellar model, the code solves the set of linear pulsation eigenequations for the user-specified pulsation mode (l,m) within the given range of radial order n, then outputs the eigenfunctions along with their corresponding set of eigenfrequencies. The GYRE algorithm searches the frequencies by creating a frequency grid within the user-defined interval, then evaluates the discriminant at each grid point (see Townsend & Teitler 2013 for a derivation of the discriminant function using the Magnus Multiple-Shooting scheme). A change in sign of the discriminant between two consecutive points indicates that a root is bracketed, and passed to the root finding routine based on the algorithm described by Brent (1973). Once the frequency is determined, the code computes the turning point of the oscillation cavity, and use it to refine the spatial grid for evaluating the eigenfunction.

GYRE is callable from within MESA to compute a set of pulsation frequencies for the output stellar model at every evolutionary step or at the end of the simulation. Stellar rotational effects can be added to the frequency computation with the options of First-order Perturbative approach and the Traditional Approximation of Rotation (Townsend et al. 2018). In this work, we impose a uniform rotation rate to the

stellar models with the TAR formalism in GYRE developed by Townsend (2005), as described in Section 1.6.2. We compute the adiabatic oscillation frequencies within the range of 3.8 μHz to 100.0 μHz in the inertial frame of reference. Radial order n is varied from -100 to -5 with the negative sign denoting g-modes. Computation is performed in the co-rotating frame, and we set the minimum number of grid points per oscillatory wavelength to be 5 to resolve the eigenfunction. An example of the GYRE inlist is given in Appendix B.

2.3 ADIPLS oscillation code

The Aarhus adiabatic oscillation package (ADIPLS; Christensen-Dalsgaard 2008), is another open-source 1-D oscillation code callable within MESA. It uses the two most prevalent numerical methods in solving pulsation equations in the 1990s: the shooting scheme and the relaxation technique, which were later developed into Magnus Multiple-Shooting scheme (used in the more recent code GYRE). Consequently, the oscillation results computed with ADIPLS differ slightly to those computed with GYRE. ADIPLS treats rotational effects with the First-order Perturbations according to the formalism of Soufi et al. (1998). Burke et al. (2011) further extended the code to compute the Second-order Perturbation effects according to the formalism of Gough & Thompson (1990), as described in Section 1.6.1. The perturbation terms are computed according to Equation 1.15 from Kjeldsen et al. (1998). The code then outputs the numerical results for each individual term. We corrected a small mathematical error in the second-order code written by Burke et al. (2011): From equation 1.16, we used the approximate expression and obtained $Q_{2lm} = \frac{l(l+1)-3m^2}{4l^2+4l}$.

In this work, we applied uniform rotation to the models using the Second-order Perturbative approach, which is shown to be more suitable for modelling rotating γ Dor stars (Ballot et al. 2010). New functions were introduced by the author to control the computation of ADIPLS second-order rotation effects through MESA. The author edited the two codes and introduced a new input file to the MESA work directory, named `inlist_pulse_controls` (see Appendix C for an example inlist). The code for creating the input file is partially taken from the MESA Summer School teaching material[2] (2012) written by Dr. Richard Townsend, which calls ADIPLS to compute pulsation frequencies of a given degree l without adding rotational effects. This new inlist file allows users to input stellar rotation rate, specify the mode scanning control parameters, and choose either the First- or the Second-order Perturbative method to use in mode calculation when adding rotational effects. The `mode_controls` namelist section can be repeated to include modes of other values of l. ADIPLS and MESA were subsequently modified to return the final set of pulsation frequencies, as illustrated in Figure 1.8, by combining all splitting term outputs according to Equation 1.15. Major changes to the codes include **i**) allowing users to

[2]MESA marketplace http://cococubed.asu.edu/mesa_market/

specify the values of azimuthal order m to be computed, **ii**) only considering uniform rotation rather than inputting a rotation profile, since the formulation adopted for second-order is only applicable to rigid rotations; and **iii**) editing MESA results outputs to take the splitting results from the First- and the Second-order Perturbative method computation into account.[3]

2.4 Benchmark models and Grids

In order to investigate the ability of g-modes to differentiate between the rotation formalisms, we used pre-computed models as fitting targets instead of real observational data. We created benchmark models with the two rotation descriptions, and we supposed the pulsation frequencies computed from these models are the 'detected' frequencies from observations. Benchmark *bench_adipls* was modelled with the Second-order Perturbative approach (hereafter 2nd Pert.), and benchmark *bench_gyre* was modelled with the Traditional Approximation of Rotation (hereafter TAR). We computed a grid of models around each benchmark with their corresponding rotation formalism, and compared the two grids to both benchmarks for further analysis. This is similar in methodology to the work by Pedersen et al. (2018), who used the g-mode pulsations of SPB stars to distinguish between the different convective overshooting descriptions.

The benchmark models were created with reference to a γ Dor star KIC 4846809 from *Kepler* data. The use of *Kepler* star as a reference was done to ensure that our γ Dor benchmark and grid parameters are based on observations. According to data from NASA exoplanet archive[4], this star has a mass of (1.556 ± 0.242) $M_\odot$ and a radius of (1.902 ± 0.550) $R_\odot$. Analysis performed by Li et al. (2019c) showed that its period spacing pattern has a gradient of (-0.007813 ± 0.000940). By fitting the results with TAR, the star was found to be pulsating in (1,0) zonal mode with radial orders from $n = -73$ to $n = -39$. It has an asymptotic spacing $\Pi_0 = (3907.538022 \pm 15)$ s and a rotation rate $\Omega/\Omega_k = (0.0491 \pm 0.0239)$. This rotation rate falls within the domains of validity of both TAR and 2nd Pert. described in Section 1.6. We used the mass, rotation rate and pulsation mode of this star to form the stellar parameters of our benchmark models, presented in Table 2.1. Since the hydrogen abundance and the overshooting parameters of KIC 4846809 were unknown, we assumed X_c to be 0.50 and the exponential overshoot f_{ov} to be 0.02. This assumption is acceptable because the benchmark required in this work can be arbitrary and it will not affect the conclusions drawn from the model comparisons. We computed the pulsation frequencies of each benchmark for (1,0) mode within the range of 3.8

[3]The original ADIPLS 'hooks' in MESA do not have functions for inputting azimuthal order m and rotation rates, nor codes for adding rotational effects. The code on second-order computation in ADIPLS only outputs the individual terms in Equation 1.15 with the azimuthal orders neglected, and the calculation results were not returned to the core frequency computation codes nor to MESA.

[4]NASA Exoplanet Archive https://exoplanetarchive.ipac.caltech.edu/

Table 2.1: Parameters of the two benchmark models, *bench_adipls* and *bench_gyre*, simulating a γ Dor star similar to KIC 4846809.

Parameter	KIC 4846809	*bench_adipls*	*bench_gyre*
Initial Mass M ($M_\odot$)	1.556 ± 0.242	1.56	1.56
Exponential overshoot f_{ov}	(unknown)	0.02	0.02
Central hydrogen abundance X_c	(unknown)	0.50	0.50
2nd Pert. Rotation rate $f_{rot}(\Omega/\Omega_k)$	0.0491 ± 0.0239	0.05	-
TAR Rotation rate $f_{rot}(\Omega/\Omega_k)$	0.0491 ± 0.0239	-	0.05

Table 2.2: Parameters for the 2nd Pert. and TAR coarse grids, computed around the benchmark models *bench_adipls* and *bench_gyre*.

Parameter	Minimum	Maximum	Step size
grid_adipls_coarse & *grid_gyre_coarse*			
Initial Mass M ($M_\odot$)	1.40	1.60	0.50
Exponential overshoot f_{ov}	0.01	0.03	0.01
Central hydrogen abundance X_c	0.48	0.52	0.01
Rotation rate $f_{rot}(\Omega/\Omega_k)$	0.00	0.14	0.02

μHz to 38.6 μHz, which is the typical observed frequency range for γ Dors. The maximum and minimum radial order n was adjusted in GYRE such that it outputs all eigenfrequencies within this range.

Two rotation grids, the 2nd Pert. grid (*grid_adipls_coarse*) and the TAR grid (*grid_gyre_coarse*), were then computed, with parameters centring around those of the benchmark model presented in Table 2.1. We followed the usual forward seismic modelling technique and varied four parameters: initial mass, central hydrogen abundance, exponential core overshooting, and rotation rate. Table 2.2 lists the parameters set-up for each grid, with rotation effects applied using 2nd Pert. and TAR respectively. Note that the initial mass of the models cannot exceed 1.60 $M_\odot$ due to our settings in MESA mesh used for resolving g-modes. Two Korn shell scripts, `run_gyre.sh` and `run_adipls.sh`, were written by the author to scan over the rotation grids (see Appendix D). The code runs over all parameter combinations within the multi-dimensional grid space defined by the user, and inputs the numbers to the MESA and GYRE or ADIPLS inlists at each run. The code then calls MESA to evolve the star and subsequently calls the pulsation code to process the final stellar model. Hereafter, we refer the stellar mass, overshooting, core hydrogen abundance, and rotation rate parameter combination of each model in our work as a *set*.

Table 2.3: List of all Grid-Benchmark pairs, including both coarse grids and fine grids, for all comparison tests completed in this work; the shorthand label used to denote each test is displayed on the right-hand side.

Pair No.	Grid	Benchmark model	Pair Label
1	*grid_adipls_coarse*	*bench_adipls*	*gAbA*
	- *gAbA_fine*	- *bench_adipls*	- *gAbAf*
2	*grid_gyre_coarse*	*bench_gyre*	*gGbG*
	- *gGbG_fine*	- *bench_gyre*	- *gGbGf*
3	*grid_adipls_coarse*	*bench_gyre*	*gAbG*
	- *gAbG_fine*	- *bench_gyre*	- *gAbGf*
4	*grid_gyre_coarse*	*bench_adipls*	*gGbA*
	- *gGbA_fine*	- *bench_adipls*	- *gGbAf*

First, we compared the grids to the benchmarks amongst the same rotation formalism to determine the number of sets in the grid which best-match the same benchmark - If the number is large, it indicates that the g-modes are incapable of precisely determining the interior properties, and vice versa. To differentiate between the two rotation descriptions, we tested the grids against the benchmarks with the alternative formalism. This creates a total of four pairs of grid-benchmark comparisons. For each pair, we computed fine grids to increase the resolution of the parameter space. This was done by applying test filtering conditions for the gradient and the intercept, then performing trial and error to minimize the two filters. We manually inspected the fit rather than automatically obtaining those with minimal χ^2 values because the χ^2 is heavily influenced by the oscillating part of the period spacing pattern. The parameters of the models found to be closest to the benchmark were used to formulate a new fine grid, and we repeated this step until we obtained best-matching models. The full parameter set-up for each fine grid are presented in Table 2.4. Table 2.3 summarizes all comparison tests carried out in this work and the labelling names assigned to denote the pair combination.

2.5 Model Selection and Analysis

The pulsation frequencies output from the stellar oscillation codes were processed by a Python code, `Plot_mode_data_grid_bench.py`, written by the author (see Appendix E). The code reads all output files from the grid and the benchmark working directory specified by the user, and obtains the period spacings for each model. Figure 2.1 shows an example plot of a small grid with four models in blue and a benchmark in orange. We consider two of the major observable aspects in the period spacings, the gradient and the average period spacing (i.e. the vertical

Table 2.4: Parameters for the four fine grids computed around the models from their corresponding coarse grids which are closest to the benchmark.

2nd Pert. fine grid with ADIPLS

Parameter	Minimum	Maximum	Step size
gAbA_fine			
Initial Mass M ($M_\odot$)	1.55	1.57	0.005
Exponential overshoot f_{ov}	0.015	0.025	0.005
Central hydrogen abundance X_c	0.49	0.51	0.005
Rotation rate $f_{rot}(\Omega/\Omega_k)$	0.04	0.06	0.005
gAbG_fine			
Initial Mass M ($M_\odot$)	1.580	1.586	0.002
Exponential overshoot f_{ov}	0.010	0.014	0.002
Central hydrogen abundance X_c	0.51	0.52	0.005
Rotation rate $f_{rot}(\Omega/\Omega_k)$	0.02	0.03	0.002

TAR fine grid with GYRE

Parameter	Minimum	Maximum	Step size
gGbG_fine			
Initial Mass M ($M_\odot$)	1.55	1.57	0.005
Exponential overshoot f_{ov}	0.015	0.025	0.005
Central hydrogen abundance X_c	0.49	0.51	0.005
Rotation rate $f_{rot}(\Omega/\Omega_k)$	0.04	0.06	0.005
gGbA_fine			
Initial Mass M ($M_\odot$)	1.59	1.60	0.005
Exponential overshoot f_{ov}	0.02	0.03	0.005
Central hydrogen abundance X_c	0.49	0.50	0.005
Rotation rate $f_{rot}(\Omega/\Omega_k)$	0.10	0.12	0.002

displacement of the curve), which are directly correlated with the stellar interior rotation rate f_{rot} and the asymptotic period spacing $\Delta\Pi_l$ described in Equation 1.11. These two characteristics are often used in research for fitting the observed frequencies with χ^2-optimization and constraining the variables l, m, f_{rot} and $\Delta\Pi_l$ (see e.g. Van Reeth et al. 2016, Li et al. 2019c), as illustrated in Figure 2.2. The fitting of dips in the curve are largely neglected in this method because **i**) we focused on the modelling of rotation effects on period spacings rather than convective mixings; and **ii**) it is difficult to observe all detailed dips in the period spacing curve from real data, we tend to only see a general trend in the spacings. For this reason, we used two filtering conditions to extract models which are sufficiently close to the benchmark – the gradient and the intercept.

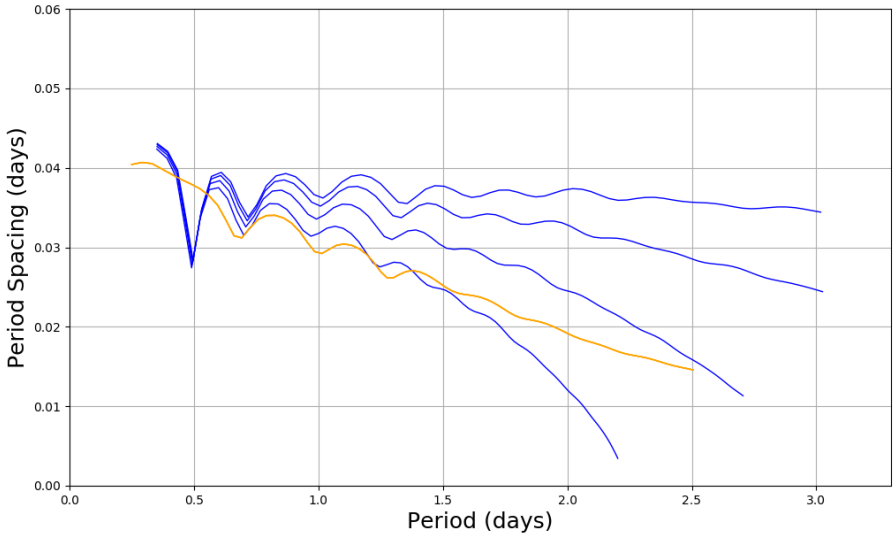

Figure 2.1: An example period spacing plot of a benchmark model (in orange) and a grid with four models varying in rotation rate (in blue). The large dips at lower periods are neglected when fitting the gradients. In this example, none of the grid models match the benchmark, hence the grid needs refining.

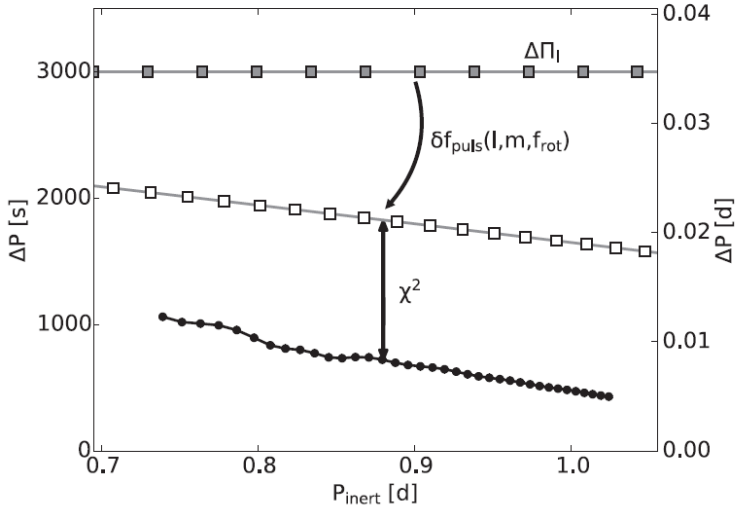

Figure 2.2: Illustration of the state-of-the-art fitting method for deriving the pulsation mode (l,m), rotation rate f_{rot} and asymptotic period spacing $\Delta\Pi_l$ from observed frequencies. An equally spaced period series is first created (grey squares), then rotation effects are applied to add a slope to the linear series (white squares). These two transformations are combined and fitted to the observed period spacing curve, optimizing for l, m, f_{rot} and $\Delta\Pi_l$. Reprinted from Van Reeth et al. (2016).

The python code performs linear fitting to the period spacing patterns of all models. It then evaluates the error in gradient and the error in intercept of the benchmark, and we define the two uncertainties to be the boundaries within which the period spacings are not differentiable. Grid models with gradients and intercepts falling within this range will be considered as indistinguishable from the benchmark, and we hereafter regard them as the *best-matching models*. For situations where perfect best-matching models could not be obtained, we focused on the gradients of the models since it is the diagnostic used in current seismic research for determining internal rotation (Ouazzani et al. 2017). We also neglected the low-period regions with large oscillations when fitting the period spacing curves, because the analysis of gradients used in research were often performed with the dips removed (Li et al. 2019c). With these best-matching models extracted from the fine grids in Table 2.4, we performed a comparison with the same formalism (internal comparison), and with the other formalism (external comparison). We examined the plots from the latter in detail to identify the period range where the curves diverge and become distinguishable. We investigated the range of parameters that produces period spacings within the gradient and intercept boundaries, then compared them against the set of the benchmark.

The χ^2 values between each benchmark and the grid models were evaluated to investigate the correlations amongst the stellar parameters. This χ^2 function compares the frequency of each mode of a grid model f_i^{grid} against the nearest frequency from their counterpart benchmark $f_i^{benchmark}$, given by

$$\chi^2 = \frac{1}{N-k} \sum_{i=1}^{N} \left(\frac{f_i^{benchmark} - f_i^{grid}}{\sigma_R} \right)^2 , \tag{2.1}$$

where N is the number of modes, k is the number of independent parameters varied in the grid, and σ_R is the error in frequency. We take σ_R as the Rayleigh limit of *Kepler* mission, 0.00068 d^{-1}, which is the upper limit for frequency error (Bowman et al. 2015). Data interpolation is performed in the code for cases where the number of modes in the grid and the benchmark are different, and we limit the frequencies to a range which is fully covered by both period spacing curves. The 2-D variations of χ^2 as a function of each parameter combination were then generated for identifying trends.

In summary, the methodology adopted in this thesis follows the common seismic modelling procedures for measuring interior rotation rates, but replacing the observed data with frequencies computed from a benchmark model that has known interior properties. Such methods provide an opportunity for us to validate the probing power of g-modes in γ Dor stars, as well as identifying the conditions of which different rotation formalisms can be distinguished.

Chapter 3

Results

This thesis aims to develop a method of determining the more suitable rotation description without knowing the rotation rate prior to fitting the period spacings with models. While previous studies have shown that both 2nd Pert. and TAR are valid formalisms at the low rotation rates used in the models of this work (e.g. Ballot et al. 2010, Townsend 2003a), our comparison results revealed that the two modelling formalisms do not agree on the rotation rate derived from their pulsation frequencies. It is therefore necessary to quantify the possible errors in the fitted stellar parameters that could arise from using an inappropriate formalism to characterise observational data. In this chapter, we present our results which compare the period spacings computed with the two formalisms at a range of rotation rates to illustrate their differences (Section 3.1). We then centred our investigation around three explicit questions: (**I**) How well do the period series of the grid models reproduce the benchmark (Section 3.2); (**II**) How can we differentiate between the period series modelled with different rotation descriptions (Section 3.3); and (**III**) Are the stellar parameters correlated (Section 3.4). We used the four sets of benchmark-grid comparisons to draw interpretations upon the best-matching models extracted from each test, and discuss on the accuracy of our modelling methodology.

3.1 Variation of Period spacings with Rotation

To illustrate the differences between the Second-perturbative method and the Traditional Approximation, we compared the pulsation frequencies computed with the two formalisms at a range of fixed rotation rates. A 1.55 $M_{\odot}$ example γ Dor model with central hydrogen abundance X_c of 0.50 and core overshooting f_{ov} of 0.03 was used in our initial comparison tests. We varied its rotation rate in the two pulsation codes, ADIPLS and GYRE, from $\Omega/\Omega_k = 0.00$ to $\Omega/\Omega_k = 0.14$, which falls within the domain of validity of both rotation formalisms. Figure 3.1 shows the period spacing pattern of this stellar model rotating at rates of $\Omega/\Omega_k = 0.00,\ 0.02,\ 0.04,\ 0.06,\ 0.08,\ 0.10,\ 0.12$ and 0.14 respectively. The blue

curve represents the results computed with 2nd Pert., and the orange curve represents those computed with TAR. At zero rotation, no observable differences can be seen in their period spacing patterns – their compute pulsation frequencies only differ in the order of 10^{-3} μHz. Both curves have negative gradients which decreases with rotation rate, and the oscillations in the curve decreases with period, in agreement with previous studies (see Section 1.5.3). Comparing the two period spacing patterns, we can see a deviation between the curves which increases with rotation rate. The major observed differences are: **i**) The gradient of the 2nd Pert. curve decreases at a rate faster than that of the TAR curve; **ii**) In contrast to the TAR curves which are generally linear, the 2nd Pert. curves bend towards lower spacings as rotation increases; and **iii**) The 2nd Pert. curves appear to break-down at rotation rates of $\Omega/\Omega_k = 0.12$ and beyond, with unrealistic pulsation periods computed when the period spacing approaches zero. There appears to be a maximum period limit in the pulsation modes computed with 2nd Pert., and this limit decreases with rotation rate.

These comparison results show that the modelling parameters obtained from applying the 2nd Pert. formalism will differ to those obtained from applying TAR. Since the slope is our current method of deriving interior rotation, modelling an observed period spacing with this gradient using the two formalisms would result in two different stellar rotation rates. This is an important finding which justifies the urge to determine a more accurate formalism for modelling the rotation of γ Dor stars. Note also that both formalisms can produce an equivalently large range of gradients provided that there is no limit to the rotation rate apart from the critical velocity. We hence eliminate the possibility of distinguishing the formalisms using their gradient ranges.

The dips in the period series are related to the star's internal mixing parameters. From Figure 3.1, it can be seen that these dips appear to shift towards lower periods as rotation increases, and in particular, the dips in the 2nd Pert. curve become increasingly compressed at low periods relative to the TAR curve. To investigate different treatments of mixing effects, we compared the location of the first largest dip in the two period spacing curves, and examined their relation to the stellar rotation rates. A python code `Plot_1st_min_rotation_adipls_gyre.py` was written by the author to extract the location of the first dip in the period spacing curve, then plot the results against their rotation rate ratio (see Appendix F). Figure 3.2 displays the rotation-dip plot of each period spacing curve presented in Figure 3.1. The plots of both TAR and 2nd Pert. curve exhibit decreasing trends, which indicates that the dips are shifting towards lower periods as rotation increases. The rate of decrease of the 2nd Pert. curve is greater than the TAR curve, implying that the dips in the 2nd Pert. curve are more tightly spaced at higher rotations relative to TAR, which agrees with the characteristics observed in Figure 3.1.

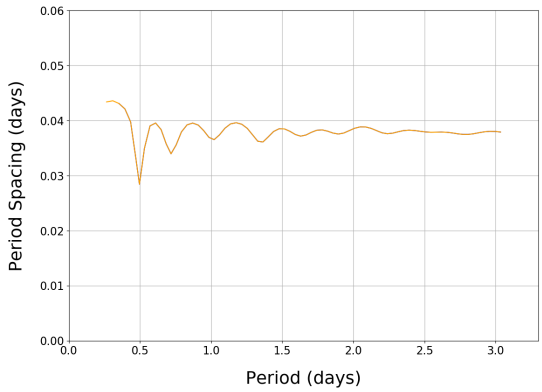

(a) $\Omega/\Omega_k = 0.00$

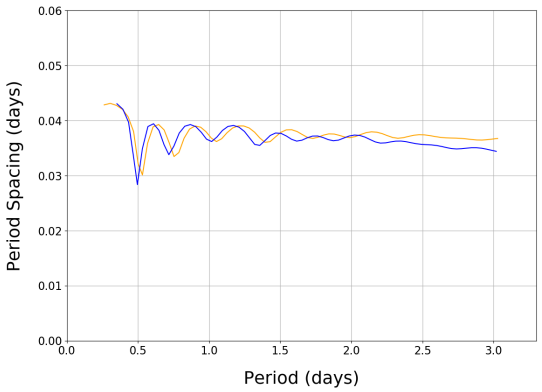

(b) $\Omega/\Omega_k = 0.02$

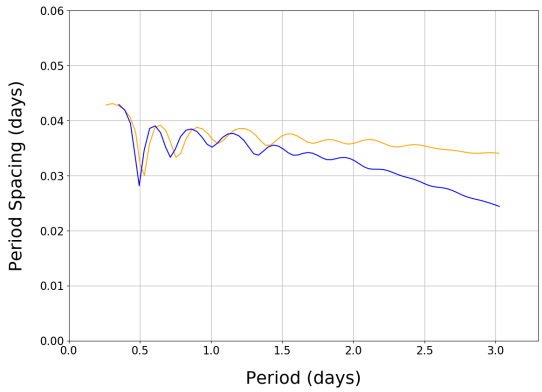

(c) $\Omega/\Omega_k = 0.04$

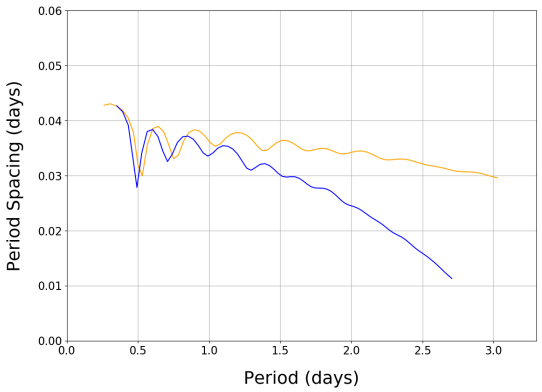

(d) $\Omega/\Omega_k = 0.06$

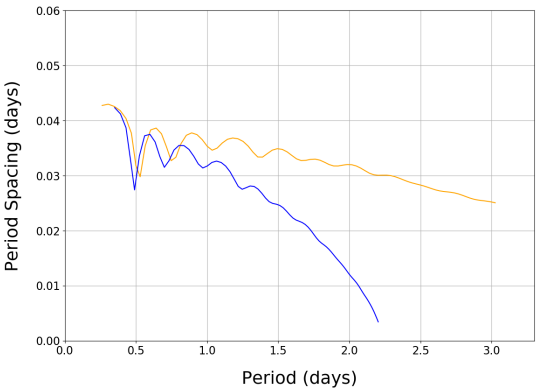

(e) $\Omega/\Omega_k = 0.08$

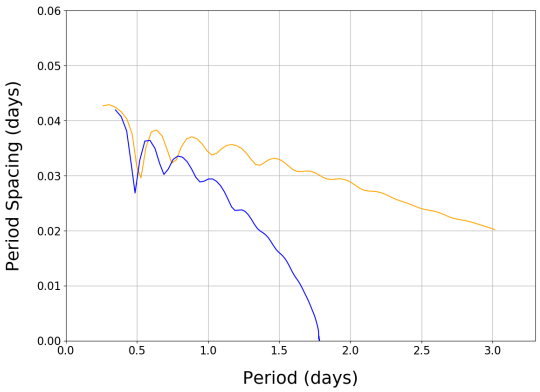

(f) $\Omega/\Omega_k = 0.10$

Figure 3.1: Pulsation period spacings of an example γ Dor model with rotation rates of $\Omega/\Omega_k =$ (a) 0.00, (b) 0.02, (c) 0.04, (d) 0.06, (e) 0.08,(f) 0.10, (g) 0.12 and (h) 0.14. The blue curve represents the period spacings computed with ADIPLS using the 2nd Pert. formalism, whereas the orange curve represents those computed with GYRE using TAR. The slope of both curves decreases with rotation, but the 2nd Pert. curve is decreasing at a faster rate than TAR. The ADIPLS rotation computation breaks down at $\Omega/\Omega_k = 0.12$ and beyond.

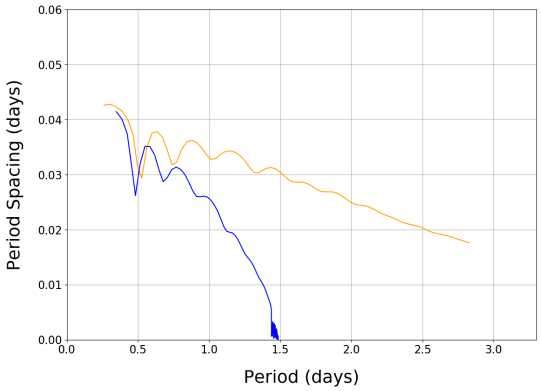

(g) $\Omega/\Omega_k = 0.12$

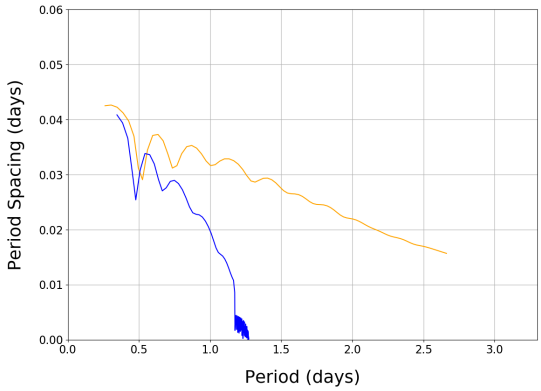

(h) $\Omega/\Omega_k = 0.14$

Figure 3.1: - *continued*

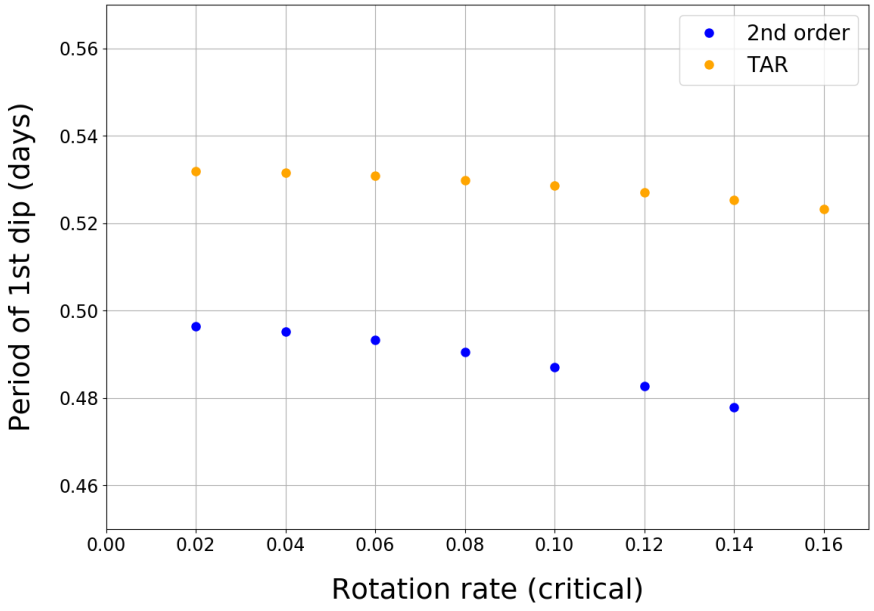

Figure 3.2: Period of the first large dip in the period spacing curve plotted against rotation rate ratio Ω/Ω_k. The blue points represent the results obtained from the 2nd Pert. curve using ADIPLS, and the orange points represent those obtained from the TAR curve using GYRE. Both plots show a decreasing trend, meaning that the dips are shifting to lower periods as rotation increases. The rate of decrease of the 2nd Pert. plot is greater than that of TAR.

The two rotation formalisms are mathematically formulated in a way such that they consequently give different descriptions to the observable effects of rotational mixings. TAR takes rotation into account when formulating the oscillation eigenfunctions, such that the amplitude of the displacement perturbation wavefunction varies as a function of rotation rate. The perturbative method does not alter the eigenfunction when rotation is added, rather, it adds additional terms to the end of each computed frequency - these terms are independent of model parameters other than the rotation rate. Hence, TAR takes into account the change in Brunt-Väisälä frequency due to mixing better than the perturbative approaches. We conclude that the TAR and the 2nd Pert. formalisms are not equally valid even at low rotation rates of below $\Omega/\Omega_k = 0.10$ due to mixing treatments.[1] The two formalisms have to be distinguished and compared to real observational data in order to determine the most accurate 1-D description of rotating γ Dor stars.

3.2 Probing power of g-mode Pulsations

To investigate Question (**I**) on the sensitivity of γ Dor pulsation frequencies, we compared the benchmarks and grids computed with the same rotation theory to ensure that both theories allow rotation rates to be precisely derived. From the fine grids *gAbA_fine* and *gGbG_fine* in Table 2.4, we extracted the best-fit models which have both gradients and intercepts falling within the uncertainty errors of the benchmark model. A substantial number of best-fit models is guaranteed since models within a localized parameter space computed with the same code and same formalism produce similar pulsation period series. We examined the parameters ranges of models that reproduce the benchmark to gauge the probing power of g-modes.

Figure 3.3 shows the period spacing plot of the 2nd Pert. benchmark (*bench_adipls*) plotted in red, and the best-matching models extracted from the 2nd Pert. fine grid (*gAbA_fine*) plotted in blue. The opacities of the curves indicate the χ^2 difference with the benchmark – the darker the line, the lower the χ^2 value and the better the fit. It can be seen that all the models at periods greater than 1.5 days are very close to the benchmark. However, at lower periods where the period series exhibit prominent sinusoidal behaviour, one of the best-matching models has dips which are significantly different to the benchmark. As dips are correlated with internal mixings, this is an indication that fitting a particular period series with gradients and intercepts may result in a best-fit model that has incorrect mixing.

To further investigate the probability of obtaining incorrect stellar properties from gradient and intercept fitting, the parameter sets of the extracted best-matching

[1] This is unlikely to be due to differences in numerical methods (e.g. the shooting schemes) employed in the two codes because such factor would result in a shift in the pulsation frequencies at zero rotation, rather than generating influences on the frequency computations which varies with the magnitude of rotation effects.

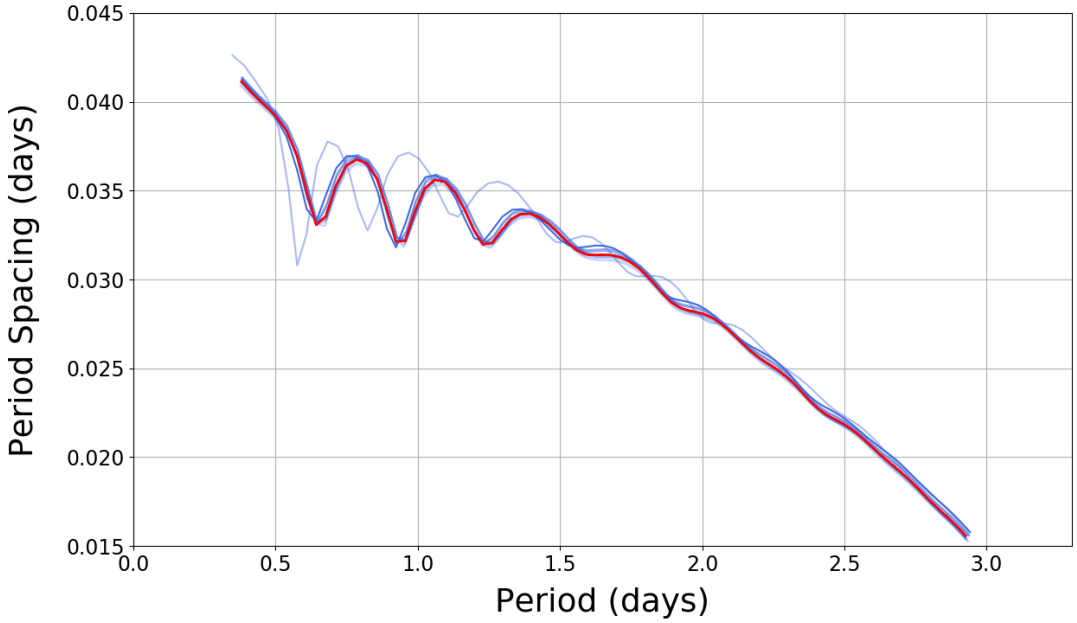

Figure 3.3: Period spacing plot of the 2nd Pert. benchmark model (in red) and the 9 best-matching models extracted from the 2nd Pert. fine grid (in blue). The opacity of the blue curves indicate the χ^2 value relative to the benchmark curve. The grids fit the benchmark very well at periods greater than 1.5 days, but one particular model does not agree with the benchmark for the dip locations at lower periods.

models are displayed in Table 3.1, ranked according to their χ^2 difference to benchmark. Here, we excluded the model which is identical to the benchmark and has a χ^2 value of zero. The rotation rates derived from the best-fit models are precise and all match the benchmark. This result is in agreement with Ouazzani et al. (2017) in which the authors found that the gradient of the period series is uniquely correlated with rotation. Model no. 6 is the only matching model which has a different overshoot parameter, leading to differences in dip locations along the period series in Figure 3.3. Its overshoot parameter only differs from the rest by one step on the fine grid, thus it is very sensitive. On the other hand, the period series of the grid models are found to be not sensitive to stellar mass and hydrogen abundance. The initial mass of the best-matching models ranges from 1.550 $M_\odot$ to 1.570 $M_\odot$ and it spans across the mass boundaries of this fine grid. This range falls within the general observational limits, which is around ± 0.2 $M_\odot$ for KIC 4846809. Since changes in both stellar mass and hydrogen abundance shift the period spacing curve vertically, it is possible that the range of these two parameters in the best-fit models are correlated with each other, and are dependent on the intercept error of the benchmark.

Table 3.1: Parameters of the 8 best-matching models extracted from comparing period spacing patterns of the 2nd Pert. fine grid models to the 2nd Pert. benchmark model.

Model	Mass M ($M_\odot$)	Exponential overshoot f_{ov}	Hydrogen abundance X_c	Rotation rate f_{rot} (Ω/Ω_k)	χ^2 diff.
1	1.565	0.020	0.495	0.05	500.98
2	1.570	0.020	0.505	0.05	949.48
3	1.570	0.020	0.500	0.05	953.00
4	1.565	0.020	0.505	0.05	992.10
5	1.565	0.020	0.500	0.05	1000.57
6	1.570	0.025	0.510	0.05	1219.96
7	1.550	0.020	0.500	0.05	1767.71
8	1.555	0.020	0.500	0.05	1785.94

Benchmark comparison results for the TAR formalism are presented in Figure 3.4. It shows the period spacing plot of the TAR benchmark (*bench_gyre*) plotted in red, and the best-matching models from the TAR fine grid (*gGbG_fine*) plotted in orange. We obtained 21 grid models falling within the uncertainty boundaries of the benchmark (excluding the identical model), which is significantly more than those extracted from the 2nd Pert. grid, despite the two grids sharing the same parameter setup. From Figure 3.4, we can also see that the best-matching models are separated into two distinct groups – one with lower χ^2 values in general, where the dips have similar locations to the benchmark, and the other one with greater χ^2 values, where dips appear to have larger amplitudes and appear 'out-of-phase' with the former. This difference in dips between the two groups of best-fit models remains prominent even at periods beyond 2.5 days. Our interpretations to this, as with the 2nd Pert. models, is that the gradient-intercept fitting method is unable to precisely probe the internal mixing parameters.

The parameters of the 21 best-matching models are presented in Table 3.2. Stellar mass ranges from 1.550 $M_\odot$ to 1.570 $M_\odot$, and the hydrogen abundance X_c ranges from 0.490 to 0.510. Similar to the results from Table 3.1, both parameters were found to have values spanning across their grid boundaries with no particular trend. The error of stellar mass was found to be at least 0.02 $M_\odot$. Whilst the actual error remains unknown, since it is well below its observational uncertainty, we consider the modelling results of stellar mass to be precise.

The rotation rates of the best-matching models are found to be slightly less precise compared to the results form the 2nd Pert. grid. The two different rotation rates obtained from fitting the benchmark model, $\Omega/\Omega_k = 0.050$ and $\Omega/\Omega_k = 0.055$, do not have strong correlations with the χ^2 values, implying that there is an error of around $\Omega/\Omega_k = 0.005$ in the derived rotation rates from the TAR formalism.

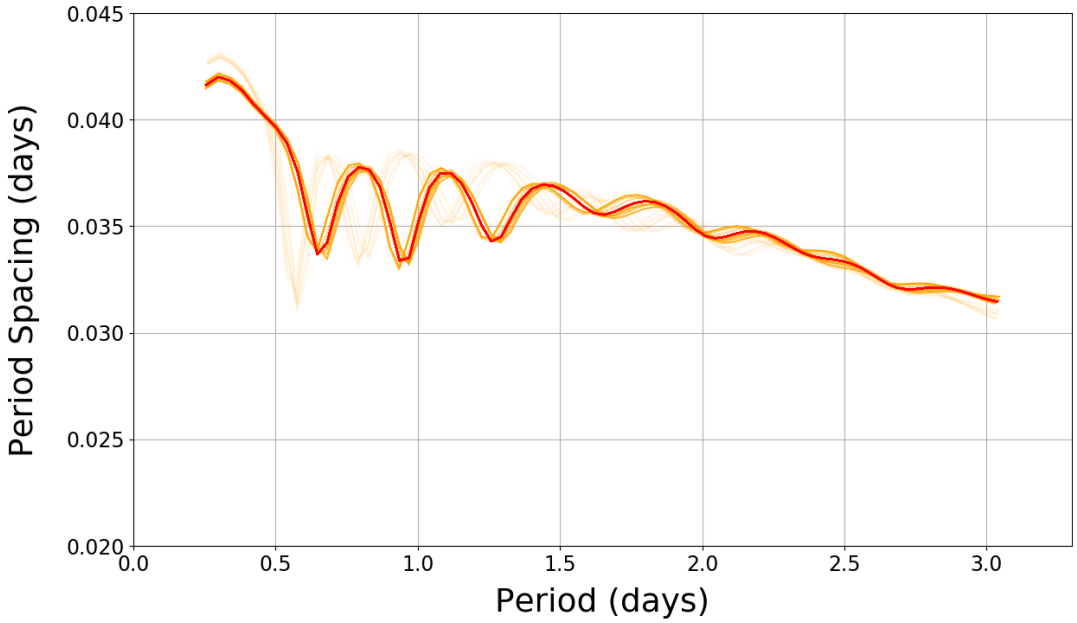

Figure 3.4: Period spacing plot of the TAR benchmark model (in red) and the 22 best-matching models extracted from the TAR fine grid (in orange). The opacity of the orange curves indicates the χ^2 value relative to the benchmark curve. The grids generally match the benchmark well especially at the longer period regions, but higher χ^2 models tend to have dip locations which appear to be 'out-of-phase' with the benchmark.

(NB: We hereafter refer the parameter values of the best-matching models that do not reproduce the benchmark as *errors*.) Compared to the observed rotation rate uncertainty of KIC 4846809 of $\Omega/\Omega_k = 0.0239$, this error is relatively small and falls within the acceptable level of accuracy. The overshooting and mixing effects in the extracted models were found to be the key aspects which influenced the ability of g-modes in reproducing the benchmark model. The 'out-of-phase' period series in Figure 3.4 correspond to models with overshooting parameters of 0.025. From Table 3.2, it can also be seen that the models with a higher and less-accurate rotation rate, $\Omega/\Omega_k = 0.055$, are the same as those with a larger convective overshooting parameter, 0.025. Both parameters do not appear to be correlated with the χ^2 values.

In summary, the grid models computed with both formalisms are generally capable of mimicking the shape of their benchmark period spacing curves. The gradient-intercept modelling method allows the stellar mass and age to be derived to within observational uncertainty. However, because this modelling method neglects the lower periods, it is unable to precisely reproduce the dips caused by overshooting.

Table 3.2: Parameters of the 21 best-matching models extracted from comparing period spacing patterns of the TAR fine grid models to the TAR benchmark model.

Model	Mass M ($M_\odot$)	Exponential overshoot f_{ov}	Hydrogen abundance X_c	Rotation rate f_{rot} (Ω/Ω_k)	χ^2 diff.
1	1.560	0.020	0.495	0.050	11.03
2	1.565	0.020	0.495	0.050	104.58
3	1.555	0.020	0.500	0.050	122.49
4	1.555	0.020	0.505	0.050	125.63
5	1.560	0.020	0.505	0.050	154.21
6	1.565	0.020	0.505	0.050	186.38
7	1.565	0.020	0.500	0.050	249.67
8	1.560	0.025	0.505	0.055	822.76
9	1.560	0.025	0.500	0.055	884.75
10	1.560	0.025	0.495	0.055	909.74
11	1.565	0.025	0.510	0.055	1101.78
12	1.565	0.025	0.500	0.055	1129.57
13	1.565	0.025	0.495	0.055	1169.22
14	1.570	0.020	0.490	0.050	4609.82
15	1.570	0.020	0.495	0.050	4637.16
16	1.550	0.020	0.505	0.050	4637.60
17	1.550	0.020	0.500	0.050	4686.44
18	1.570	0.020	0.500	0.050	4812.89
19	1.570	0.025	0.495	0.055	7751.91
20	1.570	0.025	0.490	0.055	8228.65
21	1.565	0.025	0.490	0.055	8423.75

Such error in overshoot also correlates with the error in stellar rotation for the TAR formalism. This correlation suggests that the error in the best-fit models are possibly related to the mixing treatments of the formalism, as discussed in Section 1.6.4 and Section 3.1. Both parameters induce mixing effects at the core boundaries and influence the distribution of the Brunt-Väisälä frequency. If this is true, the reason for why this correlation is not seen in the 2nd Pert. comparison test can be explained by the fact that, unlike 2nd Pert., TAR takes the eigenfunctions into account when computing rotational effects. Despite being a more accurate way of treating mixing effects, we showed that such formalism can increase the chance of obtaining an incorrect model. If overshoot influences the modelling precision of rotation, it could imply that we cannot simply consider the gradient to determine rotation rates and neglect the dips in the curve. Further investigations are required to find out how this correlation can be explained by the theoretical formulation of each rotation theory.

3.3 Using g-modes to unravel the Rotation formalisms

To answer Question (**II**) on distinguishing the different descriptions of stellar rotation, the grids are compared against a benchmark computed with the alternative formalism. Since the objective of this thesis is to model stellar rotation, we prioritized the optimization of the gradient filters over the intercept filters while extracting models from the coarse grids. However, exceptions were allowed when the gradient of the grid models were very close to the benchmark, yet the intercepts differed. An example is illustrated in Figure 3.5, where the red curve shows the benchmark, and the purple curves show the grid models which have gradients close to the benchmark at longer periods, but clearly do not fit the former. This situation happens due to the bending of the period spacing patterns in 2nd Pert. models, and they do not necessarily share the same graphical 'rotation' axis as the TAR curves (i.e. they are crossing each other). In such circumstances, it is difficult to obtain best-fit models where both their gradients and intercepts are falling within the required uncertainty errors. Instead, we presented the closest models we obtained from the fine grids, and discussed the ways of locating differences between the two period spacing curves.

Figure 3.6 shows the period spacing plot of the TAR benchmark (*bench_gyre*), plotted in red, and the 8 best-matching models extracted from the 2nd Pert. fine grid (*gAbG_fine*), plotted in blue. For low-period regions (below approximately 2.0 days), none of the best-fit grid models are capable of reproducing the period series of the benchmark. Unlike Figure 3.3 and 3.4, the spacing between each dip in the curve is much greater in the benchmark compared to the grids, indicating that there is a larger error in the modelled mixing parameters. However, the general shape of the grids' period spacing curves was found to be very similar to the benchmark, both with gradients of around -0.0034. The gradients and intercepts of the grid models at higher periods both fall within the uncertainties of the benchmark, which makes them indistinguishable by definition. If we neglect the sinusoidal component (which is difficult to accurately measure in observed data), it is hard to identify any differences between the two period series.

The parameter sets of the best-matching models are presented in Table 3.3. The most important findings from this table are the modelled rotation rates – we obtained a precise measurement of $\Omega/\Omega_k = 0.024$ from fitting the curves, which is significantly smaller than the rotation rate of the TAR benchmark, $\Omega/\Omega_k = 0.05$, by 52%. The fact that 2nd Pert. period spacings have high probing power on rotation rates (Section 3.2) shows that this difference in rotation rate is not influenced by the errors in the derived parameters due to modelling methods.

Figure 3.7 shows the period spacing plot of the 2nd Pert. benchmark (*bench_adipls*) plotted in red, and 8 TAR grid models (*gGbA_fine*) plotted in orange. The situation revealed from this comparison test is similar to that described in Figure 3.5, where

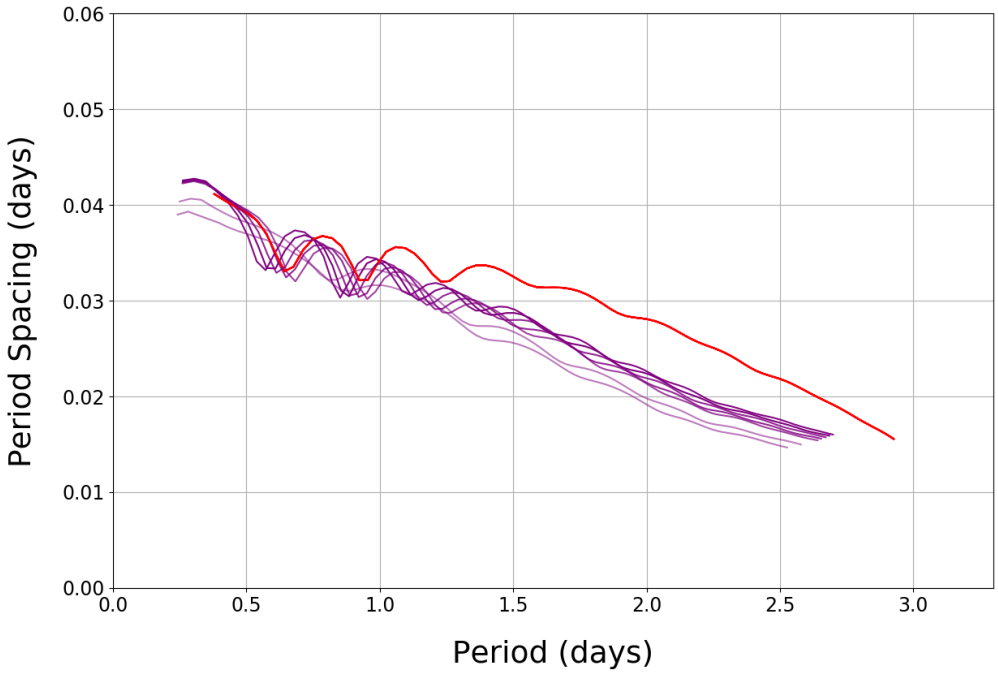

Figure 3.5: An example period spacing plot of a benchmark (in red) computed with 2nd Pert. and a grid of models (in purple) computed with TAR, extracted by prioritizing the gradient fitting. The opacity of the purple curves indicates the χ^2 value relative to the benchmark curve. The grid models do not fit the benchmark at periods greater than approximately 1.3 days despite having similar gradients; the two curves appear parallel with a large difference in the intercept points. In this example, best-fit models cannot be obtained.

we are unable to extract any best-batching models due to the shape of the curves. The grid models presented in Figure 3.7 are the closest models to the benchmark in terms of their intercept values, with a maximum period spacing difference of 0.00578 days. The gradient of the benchmark is -0.0122, which is greater than that of the benchmark curve in Figure 3.6 by 0.0088. The rotation rates of the extracted grid models range from $\Omega/\Omega_k = 0.102$ to $\Omega/\Omega_k = 0.112$. Despite the range being within observational uncertainty, it is different to the benchmark by a maximum error of 124%. At lower periods, the grid curves are found to be close to the benchmark and are generally capable of reproducing the locations of the dips. The curves begin to diverge at periods beyond 2.0 days, and such divergence becomes apparent beyond 2.5 days. As no models are falling within the benchmark gradient and average period spacing uncertainties, we consider the models in this test to be distinguishable at periods greater than around 2.5 days.

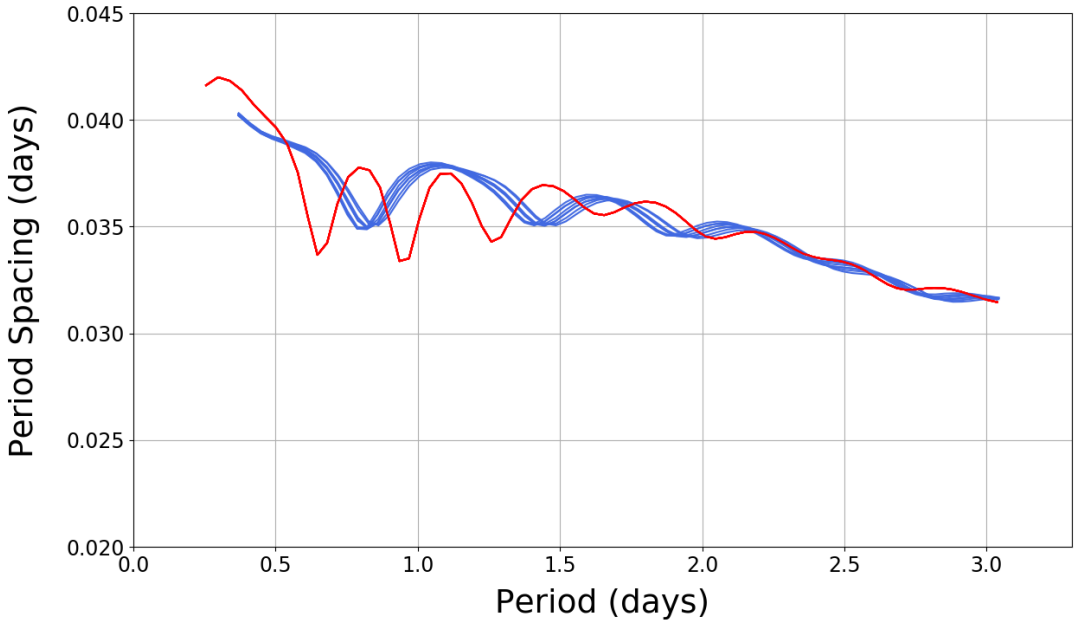

Figure 3.6: Period spacing plot of the TAR benchmark model (in red) and the 8 best-matching models extracted from the 2nd Pert. fine grid (in blue). The benchmark has a gradient of -0.0034. The dips in the period series in low-period regions are unable to mimic the benchmark. The gradients and the average period spacings of the curves computed with the two different formalisms are indistinguishable from each other.

Table 3.3: Parameters of the 8 best-matching models extracted from comparing period spacing patterns of the 2nd Pert. fine grid models to the TAR benchmark model.

Model	Mass M ($M_\odot$)	Exponential overshoot f_{ov}	Hydrogen abundance X_c	Rotation rate f_{rot} (Ω/Ω_k)	χ^2 diff.
1	1.582	0.01	0.515	0.024	2009.63
2	1.584	0.01	0.510	0.024	2039.16
3	1.584	0.01	0.515	0.024	2042.31
4	1.584	0.01	0.520	0.024	2045.35
5	1.582	0.01	0.510	0.024	2073.92
6	1.586	0.01	0.515	0.024	2077.91
7	1.586	0.01	0.520	0.024	2079.40
8	1.586	0.01	0.510	0.024	2125.46

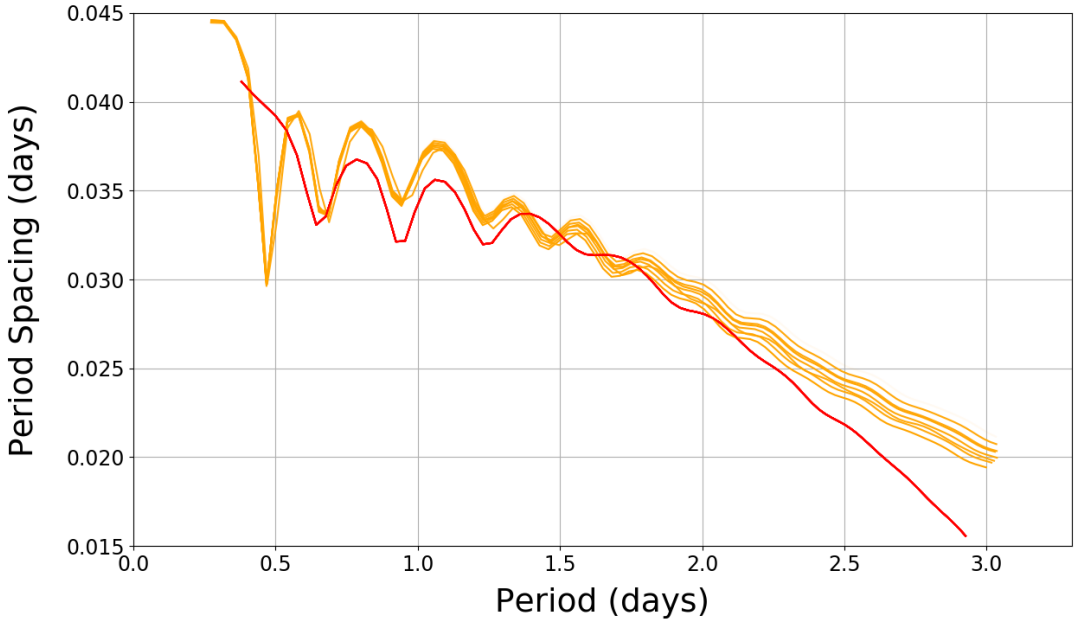

Figure 3.7: Period spacing plot of the 2nd Pert. benchmark model (in red) and the 8 models extracted from the TAR fine grid (in orange) which are found to be closest to the benchmark. The benchmark has a gradient of -0.0122. The gradient and intercept filters used in producing this plot are 0.004 and -0.00578 respectively. The grid curves fit the benchmark at periods lower than 2.0 days. Beyond this point, the curves begin to diverge.

In summary, the gradient-intercept fitting method allows the benchmark to be distinguished from the grids when its gradient is around -0.0122, but not when it is around -0.0034. The gradients of the curves have to be sufficiently large in order to see their differences as they diverge at periods greater than 2.5 days. This condition is independent of the rotation rate of the benchmark model, since they are both at $\Omega/\Omega_k = 0.5$ in the two comparison tests, yet such differences can be identified as long as the slope is substantially steep. The rotation rates between the benchmark and the derived parameter from the grids can differ up to 124%. This result is consistent with our initial comparisons presented in Section 3.1, where we have shown that period series computed with TAR and 2nd Pert. at the same rotation rate have significantly different gradients. Furthermore, the overshooting parameters in Table 3.3 are also found to be consistently lower than the benchmark by 0.01 and very sensitive to change. It is probable that this phenomenon is related to our interpretations made in Section 3.2, that the error in the derived rotation rates from the benchmark-fitting method is correlated with the error in the derived overshooting parameters.

3.4 Parameter Correlations in g-mode Pulsations modelling

We turn towards evaluating Question (**III**) on searching for correlations amongst the seismic modelling parameters. We hypothesized in Section 1.7 that the difference between the grids and the benchmark varies with the model parameters for g-mode pulsations of γ Dor stars. For instance, as rotation is increased, the gradient of the grid's period series becomes increasingly deviated from the benchmark, hence we expect to see an increase in the goodness-of-fit, χ^2. However, such correlations are not observed in the fine grids used in the comparison tests in Section 3.2 and 3.3. This is because the χ^2 values are affected by the individual dips, and this impact becomes relatively large for fine grids with small variations in parameters such as mass and rotation rate. Hence, it is difficult to identify strong correlations between them. For this reason, we used the coarse grids to compute the χ^2 differences with a benchmark and examined changes with the varied parameters in the grid. The chosen grid and benchmark are both computed with the same formalism so that we can neglect the influence from other factors such as the bending of 2nd Pert. period spacing curves relative to TAR. We considered all combinations of parameter pairs in a set, such as Mass vs. Overshoot, Mass vs. Rotation, and so on. For each combination, we extracted a portion of the data from the coarse grid for which the other two parameters in the set remained constant at values close to the benchmark. The χ^2 data were then used to generate 2-D contour plots for analysing relationships between parameters.

Figure 3.8 shows three of the six χ^2 surface plots obtained from comparing the 2nd Pert. coarse grid (*grid_adipls_coarse*; Table 2.2) to the 2nd Pert. benchmark (*bench_adipls*; Table 2.1). These were found to exhibit some correlation between the model parameters (see Appendix G for the contour plots of 2nd Pert. models that do not exhibit correlation). Contours with darker colours indicate grid models with smaller χ^2 values and better fits to the benchmark. In all three plots, the χ^2 values strongly correlate with the rotation rate of the model. The χ^2 remains small at rotation rates below approximately $\Omega/\Omega_k = 0.07$, and rise at an increasing rate from $\Omega/\Omega_k = 0.08$ to $\Omega/\Omega_k = 0.14$. This can be understood intuitively that the change in χ^2 value is dominated by the difference in gradients between the two curves, which increases at an accelerating rate with respect to rotation (Figure 3.1).

The correlations between the parameters are weak but the general trends are visible. Rotation shows a negative correlation with hydrogen abundance (i.e. positive with stellar age), and positive correlation with overshoot and stellar mass. To describe the physical significance of these surface plots, we take Figure 3.8 (b) as an example. The following deduction is explained with the help of a diagram shown in Figure 3.9. Suppose there are a few grid models which are equivalently close to the benchmark model and has the same χ^2 value. These models lie on one of the contour lines shown in the surface plot which has a positive gradient. Consider a point on

this 2-D parameter space which represents the benchmark – at $\Omega/\Omega_k = 0.05$ and $f_{ov} = 0.02$, which lies at some close distance away from the above-specified contour line. Then, suppose one of the grid models on the contour line, labelled a, has a parameter coordinate of ($\Omega/\Omega_{k_a}, f_{ov_a}$) and the other model along the line, labelled b, is ($\Omega/\Omega_{k_b}, f_{ov_b}$). Since the contour line increases with both parameters, it follows that $\Omega/\Omega_{k_b} = \Omega/\Omega_{k_a} + \delta\Omega/\Omega_k$ and $f_{ov_b} = f_{ov_a} + \delta f_{ov}$, where $\delta\Omega/\Omega_k$ and δf_{ov} represent the parameter difference between grid model a and b and they must be both positive or both negative. Hence, in most cases, Ω/Ω_{k_b} and f_{ov_b} are both further away from the benchmark parameters compared to Ω/Ω_{k_a} and f_{ov_a}. This implies that if a model has an overshoot that has a greater error, f_{ov_b}, it is likely that the rotation rate will also have a greater error, Ω/Ω_{k_b}. From the results in Section 3.2 and 3.3, we found that the best-matching models with incorrect rotation rates also have incorrect overshooting parameters. These best-matching models do not share the same χ^2, but comparing their values to the χ^2 scale in Figure 3.8 (b), they are close to lying on the same contour line. Therefore, this graphical interpretation shows (as suggested in Section 3.2 and 3.3) that the error in the derived rotation rates is correlated with the error in the overshooting parameters.

However, the correlations shown in Figure 3.8 were not observed when comparing the models computed with the TAR formalism (see Appendix G for the TAR contour plots). To the contrary of results obtained from Section 3.2, where rotation is found to be related to overshoot in TAR but not in the 2nd Pert., the surface plots showed that only the 2nd Pert. formalism exhibits relation between the parameters. Furthermore, if the above interpretation is correct, it follows that similar trends should be observed between the rotation rate and stellar mass, yet we do not see such correlation in Table 3.1 or 3.2. This implies a possibility that these χ^2 correlations are produced by coincidence, rather than by the treatments of observable mixing effects in the formalisms. Further modelling with larger parameter grids to analyse the trends on a larger scale is needed to conclude whether or not such correlation is theoretically justified.

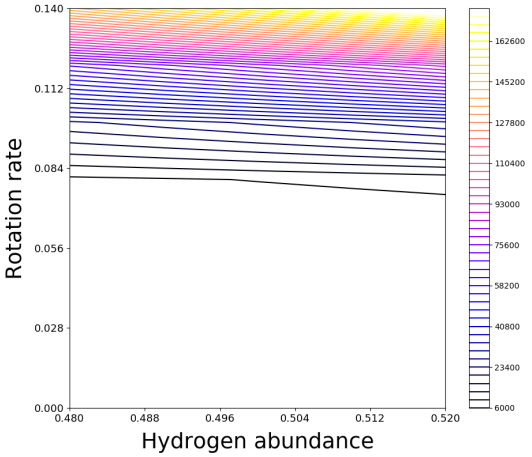

(a) rotation rate vs. hydrogen abundance

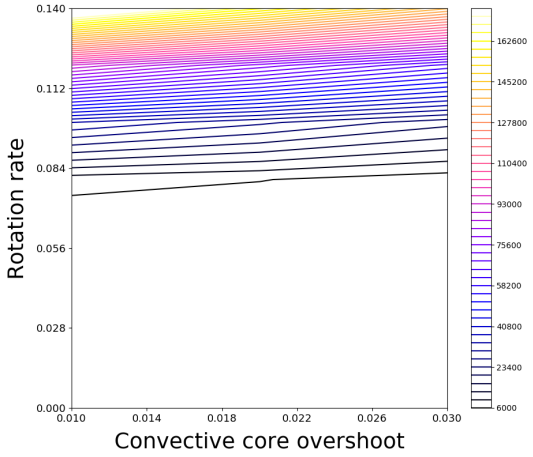

(b) rotation rate vs. overshoot

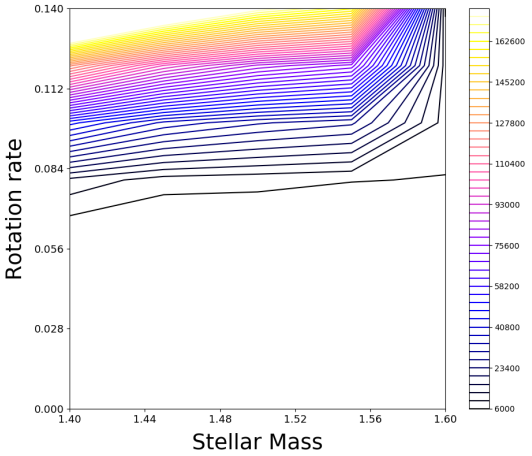

(c) rotation rate vs. stellar mass

Figure 3.8: Contour plots showing the variation of χ^2 difference between 2nd Pert. benchmark and coarse grid as a function of parameters (a) rotation rate and hydrogen abundance, (b) rotation rate and overshoot, and (c) rotation rate and stellar mass. Darker colours indicate lower χ^2 values. Rotation shows a weak negative correlation with hydrogen abundance, and weak positive correlation with overshoot and stellar mass.

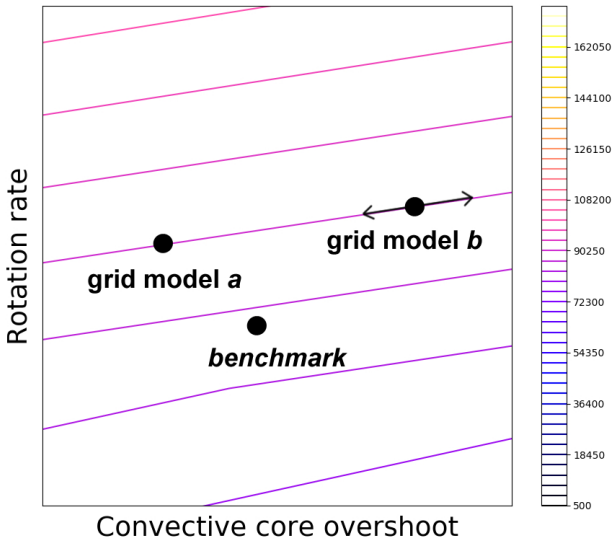

Figure 3.9: A zoomed-in contour plot of Figure 3.8 (b). This diagram illustrates how the trends observed on the contour plots justify the correlation between errors in the grid model parameters compared to the benchmark. The benchmark point is located at a certain position in this parameter space. The two points lying on the same χ^2 contour line represent two arbitrary grid models, a and b, which are equivalently close to the benchmark (roughly representing the best-fits). To evaluate the trends amongst the grid models, we think of b as a moving point along its contour line. Because the contour line has a positive gradient, it follows that, in most cases, both the rotation rate and the overshoot of the grid model would draw further away from the benchmark.

Chapter 4

Discussion and Conclusion

The gradients of the period spacing patterns of γ Dor stars reveal significant differences between the two rotation modelling descriptions examined in this thesis. Comparisons across formalisms provide information on the ways we can improve our current method of setting validity domains of rotation theories. The analysis of the best-matching models shows that our state-of-the-art seismic modelling method for deriving rotation is not sufficient for treating rotational mixing effects, and more testing is required to investigate its impact on the probing power of γ Dor g-mode pulsations. In this chapter, we use the results presented in Chapter 3 to draw interpretations to our three research questions in the context of observational asteroseismology. We discuss the limitations of the modelling methods adopted in this work and their relation to the errors in the derived stellar parameters.

4.1 Unravelling the Rotation formalisms

The difference in gradients between models computed with TAR and 2nd Pert. at the same rotation rate is one of the major findings from our study. The rotation rate that we would obtain from fitting a particular set of observed period series with 2nd Pert. is different to the rate derived if we used TAR, with percentage errors up to 124%. The gradient difference remains prominent at rotation rates down to $\Omega/\Omega_k = 0.04$. Beyond this limit, the two formalisms cannot be equally valid. The result does not comply with the domain of validity of 2nd Pert. (Ballot et al. 2010), where it is expected to be accurate for rotating stars up to $\Omega/\Omega_k = 0.3$.[1] The 2nd Pert. computation breaks down at the limit of $\Omega/\Omega_k = 0.12$. According to the modelling results of 611 *Kepler* γ Dor stars analysed by Li et al. (2019c), γ Dors have an average rotation rate of 1.106 d^{-1}. Using the average stellar mass and radius of typical γ Dors, the mean rotation ratio is around $\Omega/\Omega_k = 0.04$. This

[1]The limit established in this work is based on comparisons against TAR rather than 2-D complete calculations, but the results are not expected to differ significantly.

is at the boundary of the limit derived from our results where TAR and 2nd Pert. agree with each other. Whilst the validity domains of the two formalisms are to be more accurately defined, the uncertainty justifies our motivation to differentiate the formalisms without the use of γ Dor rotation rates.

From Section 3.3, we found that the period spacing curves computed with the two formalisms become distinguishable when their gradients are greater than -0.0122, which corresponds to a rotation rate of approximately $\Omega/\Omega_k = 0.024$ in 2nd Pert. and $\Omega/\Omega_k = 0.04$ in TAR. This result is consistent with our original understanding on the modelling of rotation, since the gradient is known to be correlated with rotation rates, and TAR is also known to be generally suitable for more rapid rotations compared to the perturbative methods. However, unlike the establishment of domains of validities in previous research (Ballot et al. 2010), this method of unravelling the formalisms is independent of our knowledge on the star's interior rotation rate. As the TAR and 2nd Pert. period series begin to diverge at periods beyond 2.5 days, their differences in shape become increasingly obvious, and we can subsequently match these models against the observed data for further comparisons and analysis. This finding satisfies the objectives outlined in our research goals, that the rotation rate is not required in the process of identifying suitable descriptions. When modelling the pulsation frequencies data from real γ Dor stars, it is no longer necessary to presuppose its interior rotation rate. We analyse the stars with long pulsation periods and large period spacing gradients to match against the models. We can then proceed to derive the star's rotation rate using the formalism which fits the observed periods better.

4.2 Validity of the Rotation modelling methods

The modern seismic modelling method for deriving rotation was found to be not sufficient for accurately probing the sinusoidal components in the period spacing curves. The method of fitting gradient and average (asymptotic) period spacing is widely employed in seismic modelling for deriving the star's interior rotation rate along with the pulsation modes (e.g. Van Reeth et al. 2016). This method is suitable for non-continuous frequency data as it neglects the dips. On the downside, it is expected to have a lower probing power on the convective overshoot properties. Our results show that the TAR models with errors in the overshoot parameter are also unable to reproduce the rotation rate of the benchmark. The analysis of the best-matching models highlights some correlations between the error in the core overshooting and the error in the derived rotation rate. An intuitive explanation to this correlation is that these errors are due to the amplitudes of the dips along the benchmark curve, which increase its gradient uncertainty, resulting in more models with a greater variation of rotation rates being extracted.

Nevertheless, the relation between the error in derived stellar rotation rates and the dips in the period spacings warrants further investigation. From Section 1.5.2, we know that the sinusoidal components in the period series mainly originate from the

effects of convective overshooting, and our model comparison results agree with this theory. Our findings on the rotating models also show that the dip locations are directly correlated with rotation rates. The shift in the dips varies with the chosen rotation formalism. This is a clear indication that, apart from overshooting, the sinusoidal components of the period series are also dependent on the treatment of rotational effects in the oscillation code or the modelling theory. It is then reasonable to make a hypothesis that this phenomenon is related to the mixing effects around the core, as we know that both convective overshoot and rotational forces introduce mixings in real stars. The level of mixing is dependent on the magnitude of the Coriolis and centrifugal forces, of which TAR and 2nd Pert. have different physical assumptions regarding the forces acting on the stellar interior as outlined in Section 1.6. Our hypothesis thereby explains why the two formalisms differ in the modelling of dips. Yet, the oscillation codes do not directly simulate mixings in the stellar model, the observable effects of mixings are mimicked as a result of the formalism's computation method. Therefore, we argue that the correlation between the error in rotation and the error in overshooting is theoretically justified, and such correlation is related to the mathematical constructions of the mixing effects as reflected in the dips.

If our hypothesis is correct, it implies that we cannot completely neglect the regions in the period series with prominent sinusoidal oscillations. Because our method removes the periods with large dips during linear fitting, we are also neglecting all observable mixing effects modelled in the frequency computation, including those induced by stellar rotation. Our work shows that this modelling technique is not sufficient for taking rotational effects fully into account. We require a method of describing the effect of rotational mixings on the pulsation period series.

4.3 Probing power of g-modes

The best-matching models extracted from the fine grids are generally capable of reproducing the benchmark parameters to within observational error, in particular, the interior rotation rates. The precision of the modelled rotations obtained from internal comparisons allow us to neglect most uncertainty in the derived rotation rates when comparing results against the alternative formalism. On the other hand, the stellar mass and core hydrogen abundance are found to be distributed randomly and less precisely probed. This is because their effects on the period series are only seen at larger scales. For example, we require the hydrogen abundance to drop from 0.5 to around 0.3 in order to produce observable changes in the average period series. To investigate the variation of stellar mass or age with the χ^2 values, we need grids with greater boundaries to eliminate the randomness in χ^2 values due to individual dips, and only consider the large-scale changes relative to the benchmark. Higher resolution grids would also improve the modelling precision, but at the expense of computational cost. Grids with step sizes that fall within the observational uncertainty give limited physical implications on the precision of the best-matching models. We are hence unable to draw solid interpretations

regarding the probing power of observed g-mode pulsation periods on the mass and the hydrogen abundance using the fine grid results. It is more appropriate to set up grids with step sizes in the order of observational uncertainties, such that we can evaluate the error contributions from the modelling method relative to the parameters' intrinsic uncertainties.

Furthermore, the dimension of the grids used in this thesis may not be not sufficient for fully modelling observed period series. Mombarg et al. (2019) showed that forward asteroseismic modelling of intermediate-mass stars is a high-dimensional problem and it requires at least 6 parameters to be varied in the grids: Stellar mass, metallicity, diffusive envelope mixing, step/exponential core overshooting, initial central hydrogen abundance, and normalized central hydrogen abundance. In our case, we need the rotation rate to be the 7th additional parameter. Hence, the probing power of the γ Dor modelling results computed in this work are limited by the number of parameters and the sizes of the grids. To investigate the full effects induced by rotation, it is necessary to incorporate the diffusive mixing parameters to reveal and isolate the rotational mixing effects involved in the frequency computations, and look at how it varies across the different rotation prescriptions.

4.4 Future Work

To validate our method of distinguishing the two rotation formalisms, an immediate step would be to select real confirmed γ Dor stars which exhibit large gradients in their pulsation period series, and look for characteristics, such as their shapes, that match the period spacing curve of models in Figure 3.7. If most of the observed data are found to be closer to one of the formalisms than the other, we may be able to conclude on the more suitable rotation theory for modelling γ Dor stars. This investigation can also be extended by considering the dipole prograde (1,1) mode, since it is the most commonly found pulsation mode identified in γ Dors (e.g. Van Reeth 2017, Li et al. 2019c). We can apply this comparison test to other formalisms used for modelling γ Dors, such as differential rotation and the 2-D complete calculations, which provide more accurate treatments for rotation. Comparisons against 2-D modelling methods can gauge the validity of the approximations adopted in 1-D oscillation codes, and determine the physical limits of where 1-D codes are no longer suitable. Our method allows such limits to be found without knowing the precise rotation rate of the star.

Investigations on the mixing effects induced by rotation are also recommended to test the hypothesis made in this thesis. The rotation formalisms, TAR and 2nd Pert., are formulated to take the effects of Coriolis and centrifugal forces into account, yet their treatments on the ways they influence the dips in the oscillation period series were never specified in their theoretical descriptions. For this reason, we hypothesized that such rotation-dependent mixing effects are modelled as a consequence of their mathematical formulations, rather than a purposeful function implemented in the code for simulating the mixings. We require a method of isolating the mixing effects

induced by rotation from the frequency computations, and find out how these effects vary with the different rotation formalisms. Explanations to such effects on the basis of stellar rotation theories would greatly improve our understanding of the physics involved in rotating γ Dor stars.

4.5 Conclusion

Stellar models do not simulate all processes occurring in stars, rather, they are formed to provide a physical view towards their observable behaviour. Comparing models with different rotation formalisms are necessary to examine their functionalities and limits, and to evaluate their ability in probing the internal properties of γ Dor stars. Using benchmark models to replace observational data acts as a powerful method for checking the validity of our modelling techniques. In this thesis, we tested the technique for deriving interior rotation, with gradient and asymptotic period spacing, which is commonly used in modern seismic research. This research aimed to develop a method which allows us to determine the most suitable formalism for any given set of observed data. We aimed to find out: (**I**) Do the grids reproduce the benchmark; (**II**) How can we differentiate the rotation formalisms; and (**III**) Are the stellar parameters correlated. The grids were generally successful in probing the benchmark parameters to within observational uncertainties. By comparing the pulsation frequencies computed with different rotation descriptions, the results reveal that $\Omega/\Omega_k = 0.04$ is the maximum limit of which the two formalisms agree with each other. Beyond this limit, the rotation rate derived from using 2nd Pert. can differ to that of TAR by up to 124%. We have shown that this modelling method is capable of distinguishing the formalisms at periods longer than 2.5 days, given that the gradients of their period spacing curves are greater than around -0.0122. Correlations between overshoot and rotation also reveal that the internal mixing effects, which are reflected as sinusoidal components in the period series, should not be neglected when modelling stellar rotation. The same research method can be applied to all other modelling techniques - we can perform a grid-benchmark test to compare the suitability of different formalisms for observed data of a similar type. These results allow us to re-establish the validity domains of the formalisms, and improve our understandings of the interior physics.

As the amount of observational data from new space missions, such as TESS (Ricker et al. 2015) and PLATO (Rauer et al. 2014), will be growing immensely over the next decade, our findings are invaluable to help formulating modelling techniques with higher accuracies and lower computational costs. With the conditions required for differentiating the formalisms known, we can focus on the frequency analysis for stars where the gradients of their period spacings are found to be sufficiently large, and identify a more suitable framework for describing the γ Dors. The well-studied stars which suits this criterion can also act as references for evaluating new pulsation and rotation theories. Therefore, the work presented in this thesis bridges the theoretical and observational aspects of asteroseismology, and provides new insights into the development of methods for refining our rotation theories.

Appendix A

MESA inlist

This is an example of the major input file, `inlist_astero.txt`, for entering the stellar parameters and other computation settings for the evolution model simulating γ Dor stars. Here, we present the inputs used for computing the benchmark models.

```
&star_job

      show_log_description_at_start = .false.
      astero_just_call_my_extras_check_model = .true.

      ! Starting model

      create_pre_main_sequence_model = .true.

      load_saved_model = .false.
      saved_model_name = 'model_21.mod'  ! ZAMS model

      save_model_when_terminate = .true.
      save_model_filename = 'FINAL.mod'

      ! Using the metallicity of Asplund et al. (2009)
      ! and OPAL type I opacity tables
      kappa_file_prefix = 'a09'
      kappa_lowT_prefix = 'lowT_fa05_a09p'
      initial_zfracs = 6

      warn_run_star_extras =.false.

      pgstar_flag = .false.
```

```
/ ! end of star_job namelist


&controls

      log_directory = 'LOGS_M_1.56_O_0.02_H_0.50_R_0.05'

      ! Initial parameters

      initial_mass = 1.56
      initial_z = 0.02
      initial_y = 0.28

      calculate_Brunt_N2 = .true.

      ! Mixing effects controls

      mixing_length_alpha = 1.8
      conv_dP_term_factor = 0
      MLT_option = 'Henyey'

      use_Ledoux_criterion = .true.
      alpha_semiconvection = 0.01
      semiconvection_option = 'Langer_85 mixing; gradT = gradr'

      ! Exponential Overshooting controls

      overshoot_f_above_burn_h_core = 0.02
      overshoot_f0_above_burn_h_core = 0.005

      set_min_D_mix = .true.
      min_D_mix = 1.0
      remove_small_D_limit = 0

      ! This value has to be lower than min_D_mix.
      D_mix_ov_limit = 5d-2

      num_cells_for_smooth_brunt_B = 0

      ! Stopping conditions - age controls and timestep controls

      max_years_for_timestep = 1d7
      min_timestep_limit = 1d-20
```

```
xa_central_lower_limit_species(1) = 'h1'
xa_central_lower_limit(1) = 0.50

! controls for output
photo_interval = 100
profile_interval = 50
history_interval = 100
terminal_interval = 5
write_header_frequency = 10
write_profiles_flag = .true.
max_num_profile_models = 500

! Mesh Controls, to resolve the g-modes near core boundary

max_allowed_nz = 20000

! global mesh resolution factor
mesh_delta_coeff = 0.2

! Additional resolution based on the P and T profiles

P_function_weight = 30
T_function1_weight = 75

! Additional resolution depending on the chemical abundances
! and gradients

xa_function_species(1) = 'he4'
xa_function_weight(1) = 80
xa_function_param(1) = 1d-2

xa_function_species(2) = 'he3'
xa_function_weight(2) = 20
xa_function_param(2) = 1d-5

mesh_dlogX_dlogP_extra(:) = 0.15
mesh_dlogX_dlogP_full_on(:) = 1d-6
mesh_dlogX_dlogP_full_off(:) = 1d-12

mesh_logX_species(1) = 'he4'

! Additional resolution near boundaries of convective regions
xtra_coef_czb_full_on = 0.0
xtra_coef_czb_full_off = 1.0

xtra_coef_a_l_nb_czb = 0.015
```

```
      xtra_dist_a_l_nb_czb = 10
      xtra_coef_b_l_nb_czb = 0.075
      xtra_dist_b_l_nb_czb = 3

      ! Properly constrain the location of convective boundaries
      convective_bdy_weight = 1
      convective_bdy_dq_limit = 1d-6
      convective_bdy_min_dt_yrs = 1d-3


/ ! end of controls namelist


&pgstar

/ ! end of pgstar namelist
```

The input file can be found on github: https://github.com/Cheryl-Lau/astero/blob/master/work_bench_adipls/inlist_astero

Appendix B

GYRE inlist

The input file, `gyre.in`, is used for entering the pulsation modes, rotation rate and other settings for the numerical methods to compute the eigenfrequencies of γ Dor stars. This is the inlist that we used for computing the TAR benchmark model.

```
&constants
/

&model
      model_type = 'EVOL'
      file = './LOGS_M_1.56_O_0.02_H_0.50_R_0.05/profile22.data.GYRE'
      file_format = 'MESA'
      uniform_rot = .true.      ! Apply a uniform rotation rate
      Omega_rot = 0.05
      Omega_units = 'CRITICAL'
/

&osc
      outer_bound = 'VACUUM'
      rotation_method = 'TAR'
/

&mode
      l = 1                     ! Spherical degree
      m = 0                     ! Azimuthal order possible to include
      n_pg_min = -100           ! Minimum radial order n
      n_pg_max = -5             ! Maximum radial order n
/
```

```
&num
      diff_scheme = 'MAGNUS_GL4'
      r_root_solver = 'BRENT'
/

&scan
      grid_type = 'INVERSE'
      grid_frame = 'COROT_I'    ! computations in corotating frame.
      freq_min_units = 'UHZ'
      freq_max_units = 'UHZ'
      freq_frame = 'INERTIAL'   ! output freqs in inertial frame
      freq_min = 3.8            ! Minimum frequency
      freq_max = 100.0          ! Maximum frequency
      n_freq = 500              ! Number of frequency points
/

&grid

      n_inner = 12  ! points in the evanescent region
      alpha_osc = 5 ! points per oscillatory wavelength
      alpha_exp = 2 ! points per exponential 'wavelength'
/


&ad_output
      summary_file = 'profile_puls_summary.txt'
      summary_file_format = 'TXT'
      summary_item_list = 'M_star,n_pg,freq,freq_units'
      mode_template = 'profile_mode.%J.txt'
      mode_file_format = 'TXT'
      mode_item_list = 'l,n_pg,omega,freq,freq_units,x,x_ref,xi_r,xi_h'
      freq_units = 'UHZ'
      freq_frame = 'INERTIAL'
/

&nad_output

/
```

The input file can be found on github: https://github.com/Cheryl-Lau/astero/blob/master/work_bench_gyre/gyre.in

Appendix C

ADIPLS inlist (coupled to MESA)

The input file, `inlist_pulse_controls.txt`, is developed by the author after editing MESA and ADIPLS to allow for pulsation frequency computation with rotational effects, using the perturbative calculation codes in ADIPLS written by Burke et al. (2011). The file is contained in all ADIPLS work directories under the edited version of MESA `astero` module. Users can enter the value of azimuthal order m and the rate of uniform rotation through this input file. When the input `in_terms_of_omega` is set to true, the code reads `angular_velocity` in units of critical rotation rate of the star (Ω_k); otherwise the code reads the rotation input in units of rad/s. Users are required to set the order of the perturbative approach preferred before adding rotational effects.

This is the inlist we used for computing the 2nd Pert. benchmark model.

```
&pulse_controls

      freqs_after_every_step = .false.
      freqs_after_final_step = .true.

/ ! end of pulse_controls namelist


&mode_controls

      l = 1
      em = -1
      nu1 = 3.0  ! microHz, inertial frame
```

```
      nu2 = 40.0
      iscan = 300
      angular_velocity = 0.05
      in_terms_of_omega_k = .true.  ! otherwise in rad/s
      compute_first_order_rotation = .false.
      compute_second_order_rotation = .true.
      special_output = 6
      save_mode_filename = 'save_M_1.56_O_0.02_H_0.5_R_0.05_mode.data'

/ ! end of mode_controls namelist
```

The modules in MESA-r10398 that are edited by the author for computing rotation effects in ADIPLS can be found on github: [`astero` module] https://github.com/Cheryl-Lau/astero and [`adipls` module] https://github.com/Cheryl-Lau/adipls. The corresponding files in the original MESA package can be replaced with these edited module files to run the computation. For details, please refer to the documentation file in https://github.com/Cheryl-Lau/astero/blob/master/README.md.

Appendix D

Shell scripts for grid scanning

The shell script for scanning ADIPLS grids, `run_adipls.f`, varies the parameters according to the user-specified boundaries and step sizes. At each iteration, it changes the parameter values in the input files `inlist_astero.txt` and `inlist_pulse_controls.txt`, then calls MESA to run the simulation. The pulsation frequency computation results are automatically saved into output files with a naming convention of `save_M_mm_O_oo_H_hh_R_rr_mode.data`, where the lowercase letters represent the values of the model's stellar mass, overshooting, core hydrogen abundance, and rotation rate respectively.

Similarly, the shell script for scanning GYRE grids, `run_gyre.f`, varies the parameter values in the input files `inlist_astero.txt` and `gyre.in`. It calls MESA to evolve the stellar model, then inputs the last model in the log directory into GYRE for frequency computation. All frequency output files are named `profile_puls_summary.txt`. The output file of each model is stored into individual directories along with the mode profiles (not required in this work). These directories have a naming convention of `gyre_output_M_mm_O_oo_H_hh_R_rr`.

The two codes can be found on github: [`run_gyre`] https://github.com/Cheryl-Lau/astero/blob/master/work_bench_gyre/run_gyre [`run_adipls`] https://github.com/Cheryl-Lau/astero/blob/master/work_bench_adipls/run_adipls.

Appendix E

Python script for processing pulsation code outputs

This python script, `Plot_mode_data_bench_grid.py`, analyses the period spacings of all models in the grid and benchmark directories specified by the user. It neglects the skipped modes in the frequency computation and only extracts the data for the specified azimuthal order m from the ADIPLS outputs. Each model is fitted with a linear curve for periods longer than 1.5 days (or 1.0 days for period series with maximum value below 1.5 days) to eliminate the oscillating regions. Their gradients and intercepts are compared against the benchmark's fitting uncertainties to extract the best-matching models. Users can opt to enter self-defined gradient and intercept filters during the testing stage. It then plots the period spacings of all best-matching models and outputs their parameter sets.

The code evaluates the χ^2 difference between all grid models and the benchmark. First, it performs data interpolation, which duplicates the data at appropriate positions which are close to the original points, such that the two curves can have the same number of frequencies for computing χ^2 with Equation 2.1. To generate the contour plots, it loops through each parameter combination, and extracts the data for each parameter and the corresponding χ^2 values from the full set of results. The extracted data from the varied parameters are those of which the other two constant parameters are at values closest to the benchmark.

The code can be found on the github website: https://github.com/Cheryl-Lau/mode-data-processing/blob/master/Plot_mode_data_bench_grid.py

Appendix F

Python script for detecting the first local minimum in period spacing patterns

This code, `Plot_1st_min_rotation_adipls_gyre.py`, processes two work directories, which only contain the models with varying rotation rates computed with each formalism. It detects the first local minimum in the period spacing curve and plots the period of this point against the rotation rate of the model.

The code can be found on the github website: https://github.com/Cheryl-Lau/mode-data-processing/blob/master/Plot_1st_min_rotation_adipls_gyre.py

Appendix G

Contour plots of χ^2 variation with stellar parameters

We present the 2-D surface plots showing the variation of χ^2 values amongst all stellar parameters, computed with the 2nd Pert. and the TAR course grids. Unlike Figure 3.8, these contours do not show smooth correlations between the two varied parameters. Note the change in scale between figures.

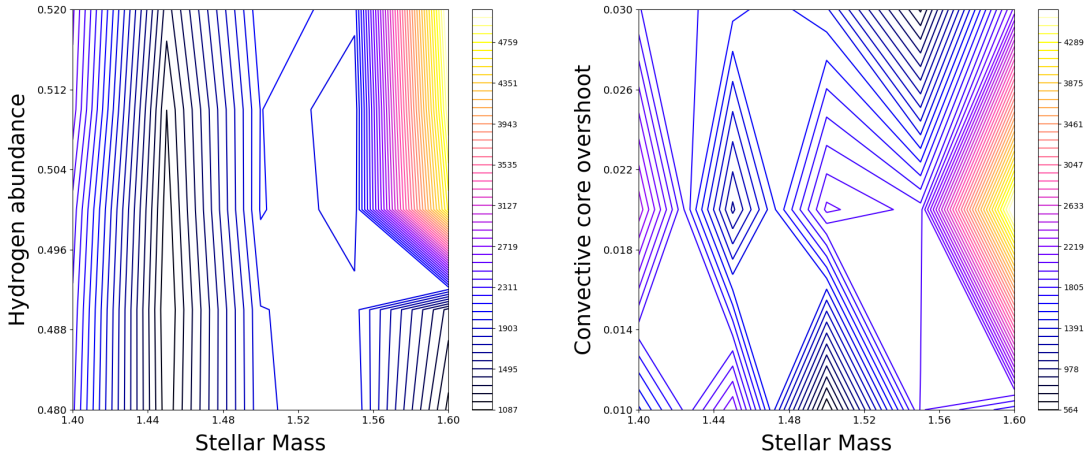

(a) hydrogen abundance vs. stellar mass

(b) overshoot vs. stellar mass

Figure G.1: Contour plots showing the variation of χ^2 difference between 2nd Pert. benchmark and coarse grid as a function of parameters (a) hydrogen abundance and stellar mass, (b) overshoot and stellar mass, and (c) hydrogen abundance and overshoot. Darker colours indicate smaller χ^2 values.

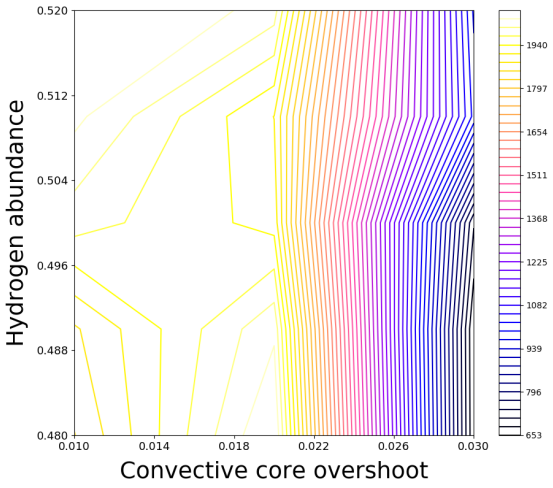

(c) hydrogen abundance vs. overshoot

Figure G.1: - *continued*

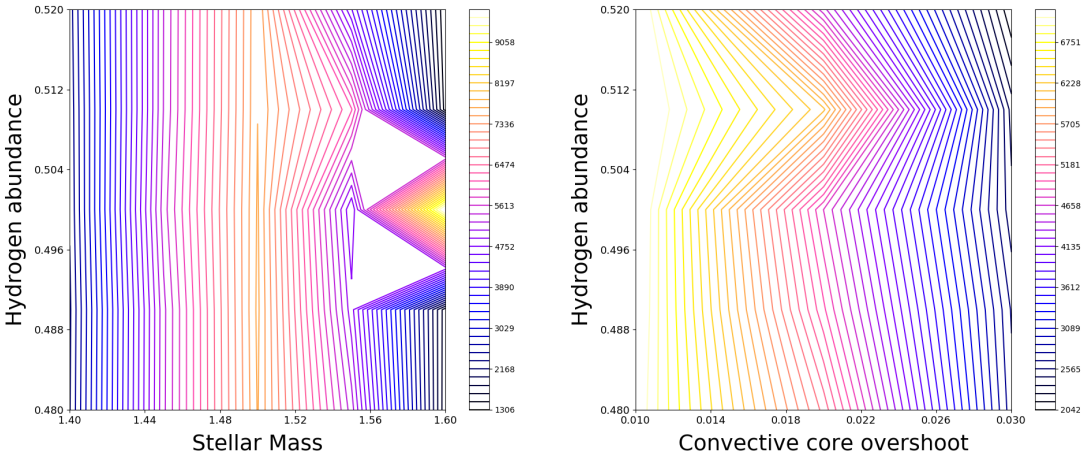

(a) hydrogen abundance vs. stellar mass

(b) hydrogen abundance vs. overshoot

Figure G.2: Contour plots showing the variation of χ^2 difference between TAR benchmark and coarse grid as a function of parameters (a) hydrogen abundance and stellar mass, (b) hydrogen abundance and overshoot, (c) overshoot and stellar mass, (d) rotation rate and hydrogen abundance, (e) rotation and stellar mass, and (f) rotation rate and overshoot. Darker colours indicate smaller χ^2 values.

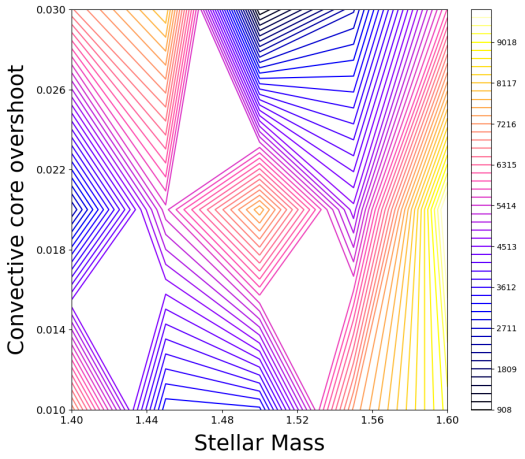

(c) overshoot vs. stellar mass

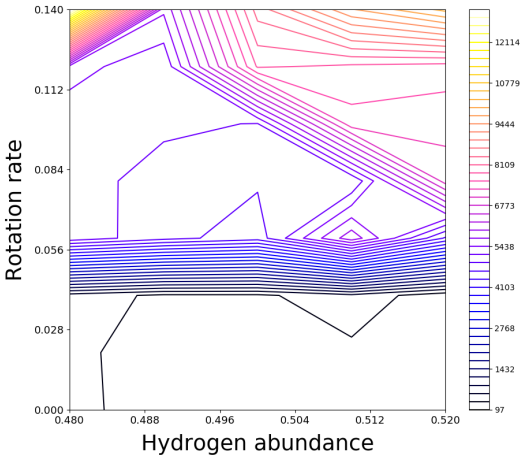

(d) rotation rate vs. hydrogen abundance

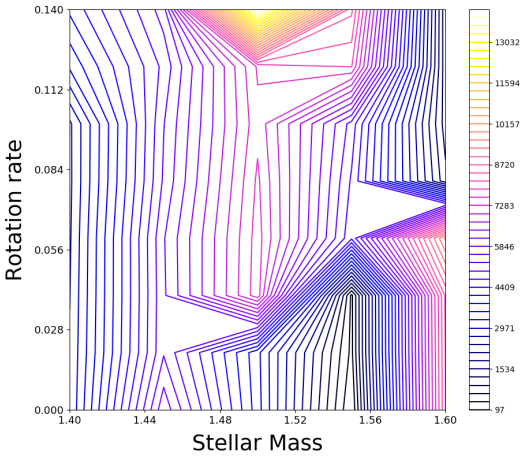

(e) rotation vs. stellar mass

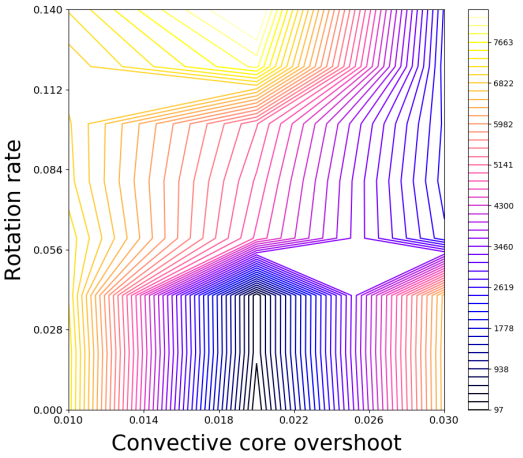

(f) rotation rate vs. overshoot

Figure G.2: - *continued*

References

Aerts, C., Christensen-Dalsgaard, J., Kurtz, D. W. (2010). Asteroseismology. Springer Publisher.

Aerts, C., Van Reeth, T., Tkachenko A. (2017). The Interior Angular Momentum of Core Hydrogen Burning Stars from Gravity-mode Oscillations. ApJL, 847, L7.

Antoci, V., Cunha, M. S., Bowman, D. M., et al. (2019). The first view of δ Scuti and γ Doradus stars with the TESS mission. MNRAS, 490, 4040–4059.

Asplund, M., Grevesse, N., Sauval, A. J., et al. (2009). The Chemical Composition of the Sun. ARA&A, 47, 481-522.

Auvergne, M., Bodin, P., Boisnard, L., et al. (2009). The CoRoT satellite in flight: description and performance. A&A, 506, 1, 411-424.

Ballot, J., Lignières F., Reese, D. R., et al. (2010). Gravity modes in rapidly rotating stars – limits of perturbative methods. A&A, 518, A30.

Ballot, J., Lignières, F., Reese, D. R., et al. (2013). Numerical exploration of oscillation modes in rapidly rotating stars. Studying stellar rotation and convection. Springer. 91-114.

Bohm-Vitense, E. (1958). Über die Wasserstoffkonvektionszone in Sternen verschiedener Effektivtemperaturen und Leuchtkräfte. Zeitschrift für Astrophysik, 46, 108.

Bouabid, M. P., Dupret, M. A., Salmon S., et al. (2013). Effects of Coriolis force on high-order g modes in γ Doradus stars. MNRAS, 429, 2500-2514.

Bowman, D. M., Holdsworth, D. L., Kurtz, D. W. (2015). Combining WASP and *Kepler* data: the case of the δ Sct star KIC 7106205. MNRAS, 449, 1004-1010.

Brassard, P., Fontaine, G., Wesemael, F., et al. (1991). Adiabatic Properties of Pulsating DA White Dwarfs. I. The Treatment of the Brunt-Väisälä Frequency and the Region of Period Formation. ApJ, 367, 601.

Brent, R. P. (1973). Algorithms for Minimization without Derivatives. Prentice-Hall, Englewood Cliffs.

Burke, K. D., Reese, D. R., Thompson, M. J. (2011). On the effects of rotation on acoustic stellar pulsations: validity domains of perturbative methods and close frequency pairs. MNRAS, 414, 1119-1126.

Burke, K. D., Thompson, M. J. (2006). The effects of rotation on the frequency of stellar oscillations. Proceedings of SOHO 18/GONG 2006/HELAS I. Beyond the spherical sun. ESA SP-624.

Christensen-Dalsgaard, J. (2003). Lecture Notes on Stellar Oscillations. 5th Ed. Institut for Fysik og Astronomi, Aarhus Universitet.

Christensen-Dalsgaard, J. (2008). ADIPLS—the Aarhus adiabatic oscillation package. Astrophys. Space Sci., 316, 113–120.

Christensen-Dalsgaard, J., Gough, D. O. (1976). Towards a heliological inverse problem. Nature, 259, 89-92.

Cowling, T. G., M. A., Phil, D. (1941). The Non-radial Oscillations of Polytropic Stars. MNRAS, 101, 8, 367-375.

Dupret, M.-A. (2018). Current problems in stellar pulsation theory. Physics of oscillating stars – a conference in honour of Prof. H. Shibahashi.

Dupret, M.-A., Grigahcène, A., Garrido, R., et al. (2005a). Time-dependent convection seismic study of five γ Doradus stars. MNRAS, 360, 1143-1152.

Dupret, M.-A., Grigahcène, A., Garrido, R., et al. (2006). Theoretical aspects of g-mode pulsations in gamma Doradus stars. Memorie della Società Astronomica Italiana, 77, 366.

Dupret, M.-A., Miglio, A., Grigahcène, A., et al. (2007). Theoretical aspects of g-mode pulsations in γ Doradus stars. Communications in Asteroseismology, 150, 98.

Eckart, C. (1960). Hydrodynamics of Oceans and Atmospheres. Pergamon Press, Oxford. Eddington, A. S. (1917). The pulsation theory of Cepheid variables. The Observatory, 40, 290-293.

Eggenberger, P., Lagarde, N., Miglio, A., et al. (2017). Constraining the efficiency of angular momentum transport with asteroseismology of red giants: the effect of stellar mass. A&A, 599, A18.

Fossat, E., Boumier, P., Corbard, T., et al. (2017). Asymptotic g modes: Evidence for a rapid rotation of the solar core. A&A, 604, A40.

Fuller, J., Piro, A. L., & Jermyn, A. S. (2019). Slowing the spins of stellar cores. MNRAS, 485, 3661-3680.

Gabriel, M. (1996). Solar oscillations: theory. Bulletin of Astron. Soc. India, 24, 233.

García, R. A., Ballot, J. (2019). Asteroseismology of solar-type stars. Living Rev. Sol. Phys 16:4.

Gough, D. O. (1983). Helioseismology: Oscillations as a probe of the Sun's interior. Nature, 304, 689-690.

Gough, D. O., Leibacher, J. W., Scherrer, P. H., et al. (1996). Perspectives in Helioseismology. Science, 272, 5266, 1281-1283.

Gough, D. O., Thompson, M. J. (1990). The effect of rotation and a buried magnetic field on stellar oscillations. MNRAS, 242, 25-55.

Grigahcène, A., Dupret M.-A, Gabriel M., et al. (2005). Convection-pulsation coupling. I. A mixing-length perturbative theory. A&A, 434, 1055-1062.

Guzik, J. A., Kaye, A. B., Bradley, P. A., et al. (2000). Driving the gravity-mode pulsations in γ Doradus variables. ApJ, 542, L57-L60.

Handler, G. (1999). The domain of γ Doradus variables in the Hertzsprung-Russell diagram. MNRAS, 309, L19-L23.

Henyey, L., Vardya, M. S., & Bodenheimer, P. (1965). Studies in Stellar Evolution. III. The Calculation of Model Envelopes. ApJ, 142, 841.

Kaye, A. B., Handler, G., Kriscuinas, K., et al. (1999). γ Doradus Stars: Defining a New Class of Pulsating Variables. ASP, 111, 840-844.

Kjeldsen, H., Arentoft, T., Bedding, T. R., et al. (1998). Asteroseismology and stellar rotation. Proceedings of SOHO 6/GONG 98 workshop. Structure and dynamics of the interior of the sun and sun-like stars. ESA SP-418, 385-390.

Koch, D. G., Borucki, W. J., Basri, G., et al. (2010). *Kepler* Mission Design, Realized Photometric Performance, and Early Science. ApJL, 713, 2, L79-L86.

Kurtz, D. W., Saio, H., Takata, M., et al. (2014). Asteroseismic measurement of surface-to-core rotation in a main-sequence A star, KIC 11145123. MNRAS, 444, 102–116.

Ledoux, P. (1949). Contributions à l'Etude de la Structure Interne des Etoiles et de leur Stabilité. Mem. Soc. R. Sci. Liège, 4(9), 3-294.

Lee, U. (2013). Low-frequency oscillations in rotating stars. Studying stellar rotation and convection. Springer. 133-158.

Lee, U., Saio, H. (1997). Low-Frequency Nonradial Oscillations in Rotating Stars. I. Angular Dependence. ApJ, 491, 839-845.

Li, G., Van Reeth, T., Bedding, T. R., et al. (2019c). Gravity-mode period spacings and near-core rotation rates of 611 γ Doradus stars with *Kepler*. MNRAS, 491, 3586–3605.

Lovekin, C. C., Guzik, J. A. (2017). Convection and overshoot in models of γ Doradus and δ Scuti stars. ApJ, 849, 1.

Maeder, A., Zahn, J.-P. (1998). Stellar evolution with rotation. III. Meridional circulation with MU -gradients and non-stationarity. A&A, 334, 1000-1006.

Mathis, S., Prat, V. (2019). The traditional approximation of rotation, including the centrifugal acceleration for slightly deformed stars. A&A, 631, A26.

Miglio, A., Montalban, J., Noels A., et al. (2008). Probing the properties of convective cores through g modes: high-order g modes in SPB and γ Doradus stars. MNRAS, 386, 1487-1502.

Mitalas, R. (1972). On Semiconvection. ApJ, 177, 693.

Mombarg, J. S. G., Van Reeth, T., Pedersen, M. G., et al. (2019). Asteroseismic masses, ages, and core properties of γ Doradus stars using gravito-inertial dipole modes and spectroscopy. MNRAS, 485, 3248-3263.

Moravveji, E., Aerts, C., Papics, P. I., et al. (2015). Tight asteroseismic constraints on core overshooting and diffusive mixing in the slowly rotating pulsating B8.3V star KIC 10526294. A&A, 580, A27.

Ouazzani, R.-M., Marques, J. P., Goupil, M.-J., et al. (2019). γ Doradus stars as a test of angular momentum transport models. A&A, 626, A121.

Ouazzani, R.-M., Salmon, S. J. A. J., Antoci, V., et al. (2017). A new asteroseismic diagnostic for internal rotation in γ Doradus stars. MNRAS, 465, 2, 2294-2309.

Papaloizou, J., Pringle, J. E. (1978). Non-radial oscillations of rotating stars and their relevance to the short-period oscillations of cataclysmic variables. MNRAS, 182, 3, 423-442.

Pápics, P. I. (2013). Observational asteroseismology of B-type stars on the main sequence with the CoRoT and *Kepler* satellites. Doctoral thesis. Institute of Astronomy Publications. KU Leuven - Faculty of Science.

Paxton, B., Bildsten, L., Dotter, A., et al. (2011). MESA. ApJS, 192, 3.
Paxton, B., Cantiello, M. Arras, P., et al. (2013). MESA. ApJS, 208, 4.
Paxton, B., Marchant, P., Schwab, J., et al. (2015). MESA. ApJS, 220, 15.
Paxton, B., Schwab, J., Bauer, E. B., et al. (2018). MESA. ApJS, 234, 2.
Pedersen, M. G., Aerts, C., Papics, P. I., et al. (2018). The shape of convective core overshooting from gravity-mode period spacings. A&A, 614, A128.
Prat, V., Mathis, S., Lignières, F., et al. (2016). Period spacing of gravity modes strongly affected by rotation- going beyond the traditional approximation. A&A, 598, A105.
Rauer, H., Catala, C., Aerts, C., et al. (2014). The PLATO 2.0 mission. Exp. Astron., 38, 249-330.
Reese, D., Lignières, F., Rieutord, M. (2006). Acoustic oscillations of rapidly rotating polytropic stars – II. Effects of the Coriolis and centrifugal accelerations. A&A, 455, 621-637.
Ricker, G. R., Winn, J. N., Vanderspek, R., et al. (2015). Transiting Exoplanet Survey Satellite, J. Astron. Telesc. Instrum. Syst., 1(1), 014003.
Rogers, F. J., Nayfonov, A. (2002). Updated and Expanded OPAL Equation-of-State Tables: Implications for Helioseismology. ApJ, 576, 1064-1074.
Saio, H. (1981). Rotational and tidal perturbations of nonradial oscillations in a polytropic star. ApJ, 224, 229-315.
Saio, H., Kurtz, D. W., Murphy, S. J., et al. (2018a). Theory and evidence of global Rossby waves in upper main-sequence stars: r-mode oscillations in many *Kepler* stars. MNRAS, 474, 2, 2774-2786.
Schmid, V. S. (2016). Asteroseismic studies of two binary systems containing pulsating components. Doctoral thesis. Institute of Astronomy Publications. KU Leuven - Faculty of Science.
Schmid, V. S. Aerts., C. (2016). Asteroseismic modelling of the two F-type hybrid pulsators KIC 10080943A and KIC 10080943B. A&A, 592, A116.
Shibahashi, H. (2005). Theory of Asteroseismology. J. Astrophys. Astr., 26, 139–160.
Silva Aguirre, V., Ballot, J., Serenelli, A. M., et al. (2011). Constraining mixing processes in stellar cores using asteroseismology. A&A, 529, A63.
Soufi, F., Goupil, M. J., Dziembowski, W. A. (1998). Effects of moderate rotation on stellar pulsation – I. third order perturbation formalism. A&A, 334, 911-924.
Tassoul, M. (1980). Asymptotic Approximations for Stellar Non-radial Pulsations. ApJS, 43, 469-490.
Townsend, R. H. D. (2000). Surface trapping and leakage of low-frequency g modes in rotating early-type stars - II. Global analysis. MNRAS, 319, 289.
Townsend, R. H. D. (2003a). Asymptotic expression for the angular dependence of low-frequency pulsation modes in rotating stars. MNRAS, 340, 1020-1030.
Townsend, R. H. D. (2005). Influence of the Coriolis force on the instability of slowing pulsating B stars. MNRAS, 360, 465-476.
Townsend, R. H. D. (2013). The pulsation-rotation interaction: greatest hits and the B-side. IAU symposium, 301.

Townsend, R. H. D., Goldstein, J., Zweibel, E. G. (2018). Angular momentum transport by heat-driven g-modes in slowly pulsating B stars. MNRAS, 475, 879–893.

Townsend, R. H. D., Teitler, S. A. (2013). GYRE: an open-source stellar oscillation code based on a new Magnus Multiple Shooting scheme. MNRAS, 435, 3406–3418.

Unno, W., Osaki, Y., Ando, H., et al. (1989). Nonradial oscillations of stars. University of Tokyo Press, 2nd ed.

Van Reeth, T. (2017). Asteroseismology of γ Doradus stars with the *Kepler* space mission. Doctoral thesis. Institute of Astronomy Publications. KU Leuven - Faculty of Science.

Van Reeth, T., Mombarg, J. S. G., Mathis, S., et al. (2018). On the sensitivity of gravito-inertial modes to differential rotation in intermediate-mass main-sequence stars. A&A, 618, A24.

Van Reeth, T., Tkachenko, A., Aerts, C. (2016). Interior rotation of a sample of γ Doradus stars from ensemble modelling of their gravity-mode period spacings. A&A, 593, A120.

Van Reeth, T., Tkachenko, A., Aerts, C., et al. (2015). Gravity-mode period spacings as seismic diagnostic for a sample of γ Doradus stars from *Kepler* space photometry and high-resolution ground-based spectroscopy. ApJS, 218, 2.